Nucleic Acids Research, 2026, **54**, gkag294
https://doi.org/10.1093/nar/gkag294
Gene regulation, Chromatin and Epigenetics

Developmental stage dominates cell-type identity and reveals a chromatin regulatory function for Rad50 in *Drosophila*

Thomas Boutet[1,2,3,4,5], Rosy Sakr[1,2,3,4,6], Marta Marzullo[7,8], Manisha Goyal[9,10], Pierre B. Cattenoz[1,2,3,4], Laura Ciapponi[7], Tina Mukherjee[10], Angela Giangrande[1,2,3,4,*]

[1]Institut de Génétique et de Biologie Moléculaire et Cellulaire, 67400, Illkirch-Grafenstaden, France
[2]Centre National de la Recherche Scientifique, 67400, Illkirch-Graffenstaden UMR7104, France
[3]Institut National de la Santé et de la Recherche Médicale, 67400, Ilkirch-Graffenstaden U1258, France
[4]Université de Strasbourg, 67000, Strasbourg, France
[5]Institut de Biologie Moléculaire et Cellulaire, UPR9022, 67084, Strasbourg, France
[6]Present address: Laboratory of Genome Integrity, CCR, NCI, NIH, Bethesda, MD, USA
[7]Department of Biology and Biotechnologies, Sapienza University of Rome, Rome 00185, Italy
[8]IBPM CNR c/o Department of Biology and Biotechnology, Sapienza University of Rome, Rome 00185, Italy
[9]The University of Trans-Disciplinary Health Sciences & Technology (TDU), Bengaluru, Karnataka 560064, India
[10]Institute for Stem Cell Science and Regenerative Medicine (inStem), GKVK, Bellary Road, Bangalore 560065, India

*To whom correspondence should be addressed. Email: angela@igbmc.fr

Abstract

Cell types are fundamental units of metazoans, however, their definition remains a long-standing challenge. We here use high-throughput assays allowing for unprecedented resolution to analyze and compare the transcriptional landscapes of related and unrelated *Drosophila* cell types at larval and embryonic stages. Unexpectedly, all cell types share a stage-specific signature that is even stronger than the cell-specific one. Despite having distinct developmental origins and functions, neurons, glia, and hemocytes are more transcriptionally similar to one another within the same developmental stage than they are to the same cell type at different stages. This stage-specific signature is enriched for DNA repair genes at larval stage, particularly the MRN complex (Mre11–Rad50–Nbs). Loss of Rad50 disrupts histone modification patterns and causes inappropriate reactivation of embryonic gene expression programs in larval central nervous system (CNS), as revealed by transcriptomic and chromatin accessibility analyses. The identification of cell-specific and stage-specific signatures highlights a new dimension in the definition of cell identity and suggests a role for Rad50 in maintaining developmentally appropriate chromatin states.

Graphical abstract

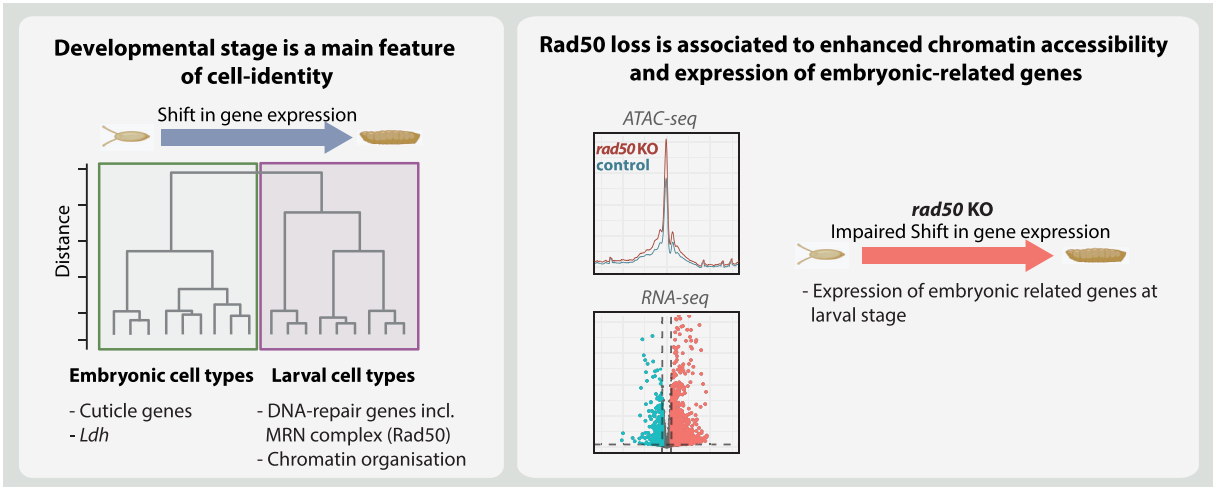

Received: December 18, 2025. **Revised:** February 25, 2026. **Accepted:** March 5, 2026

Introduction

The definition of cell identity remains a fundamental challenge in biology [1–4] and the question of what defines a cell type becomes particularly complex when considering development. Differentiated cells must maintain their core identity while simultaneously adapting to changing developmental contexts. RNA-sequencing assays have recently identified the transcriptional landscapes of three *Drosophila* cell types: neurons, glia, and hemocytes [5]. Neurons and glia share a common ectodermal origin but perform distinct functions: neurons transmit information and secrete neuropeptides; glia support nervous system development, establish the blood-brain barrier, and provide immune functions within the nervous system [6–8]. Hemocytes, derived from mesoderm, patrol the organism to ensure cellular immunity [9–11], thus sharing immune function—but not developmental origin—with glia and sharing neither origin nor function with neurons. Comparing two stages at which the different cell types are fully functional, late embryo (E16) and wandering third instar larva (L3 for the sake of simplicity) allowed the identification of the most robust cell-specific signatures [5].

In this study, we extend this analysis and reveal an unexpected property of cells: stage represents the dominant source of transcriptional variation, even more than cell type. For example, embryonic neurons are more similar to embryonic glia and hemocytes than to larval neurons. This finding associates with a stage-specific transcriptomic asymmetry. Embryonic-specific genes are numerous but lack functional convergence, consistent with each cell type primarily executing its own lineage specification and differentiation programs at this stage. By contrast, a smaller set of larval-specific genes converges on shared biological processes, particularly DNA repair and chromatin organization, suggesting that larval cells adopt a common genome maintenance program independently of cell-type identity. The strong enrichment of transcripts of DNA repair genes includes the MRN complex (Mre11–Rad50–Nbs) at L3. The MRN complex is evolutionarily conserved from bacteria to eukaryotes and plays essential roles in genome maintenance through the catalytic nuclease activity of Mre11 and the ATPase function of Rad50 [12, 13]. In *Drosophila*, the MRN complex is critical for genome stability during early development. Before cellularization, when gap phases are absent [14] and DNA repair processes are attenuated, it maintains telomere integrity and prevents chromosome fusions that would lead to mitotic failure and developmental arrest [15–19].

Recent work has revealed noncanonical functions for Rad50 in other systems. In mammals, Rad50 facilitates DNA demethylation during cell reprogramming, suggesting a role in establishing chromatin states during cellular transitions [20]. In yeast, the MRN-complex homologue MRX associates with chromatin boundaries and influences genome organization, thereby affecting transcriptional regulation [21].

Consistent with these findings and extending their impact, we show that loss of Rad50 leads to changes in histone mark distribution in polytene chromosomes, a widely used *in vivo* model to analyze chromatin organization. Importantly, we also show that Rad50 serves similar chromatin and transcriptional regulatory functions during larval development, through proteomic, transcriptomic, and chromatin accessibility approaches. Altogether, our findings establish developmental stage as a major determinant of cellular transcriptional programs and uncover a novel function for Rad50 in maintaining proper stage-specific chromatin states.

Materials and methods

Fly strains and genetics

Flies were raised on standard medium at 25°C. Fly strains used are: $rad50^{\Delta 5.1}$ [15, 16], w^{1118}. w^{1118} was used as controls (referred to as control in the text).

Preparation of $rad50^{\Delta 5.1}$ and w^{1118} CNS RNA-seq samples and sequencing

Mixed sexed L3 CNS (10 per replicate, 3 replicates per genotype) were quickly dissected on ice in phosphate-buffered saline (PBS), put directly in 50 µl TRIzol™ (Invitrogen, ref 15596026) once a full sample was collected and stored on ice. CNS were lysed with 10 strokes of microtube pestle (pestle was rinsed with another 250 µl TRIzol™), vortex at full speed for 1 min, and incubate 10 min at room temperature (RT) for full lysis. 1/5 V of Chloroform was added and samples were vortexed 1 min at full speed, incubated 5 min at RT, and centrifuged at 16 000 × *g* for 30 min at 4°C. Supernatant was collected, and RNA was extracted with 1V of isopropanol and glycogen (3 µg/ml final concentration), incubate at −20°C for 2 h and centrifuge at 16 000 × *g* for 30 min at 4°C. Pellets were washed twice in ethanol 75%, 15 min at 16 000 × *g* 4°C, allowed to dry quickly, resuspend in 30 µl H2O, treated with 25U DNAse I (Thermo Scientific™ 89836) for 5 min in 50 lL total volume at RT. RNA was extracted a second time in 500 µl TRIzol™ like previously described. End washing steps were performed three times. Total RNA was resuspended in 15 µl H_2O, 2 µl were kept for downstream analysis and samples were immediately stored at −80°C until processing. RNA integrity was analyzed on Agilent RNA Chip on bioanalyzer 2100 before sequencing. Library preparation and sequencing were performed at the GenomEast platform (IGBMC) using the Illumina® Stranded mRNA Prep and the illumina NextSeq 2000 system in single-end 50 bp. Number of reads obtained, and mapping stats are provided in Supplementary File S1.

RNA-seq analysis

Alignment was performed against dm6 genome using HISAT2 version 2.2.1 standard parameters specifying –rna-strandness R [22]. Counts were obtained with featureCounts [23] Version 2.0.1 with option -t exon -s 2 using r6.43 annotation file. Differential expression analysis was performed using DESeq2 [24, 25] version 1.32.0. *P*-value was corrected using Benjamini and Hochberg method and fold change was corrected using the shrinkage estimator apeglm [26]. If not specified otherwise, differentially expressed genes were considered with fold change >2 and adjusted *P*-value <.01.

RNA-seq of hemocytes, glia, and neurons were analyzed with following design = ∼ cellType + stage + cellType:stage. Fold changes correction was applied using apeglm algorithm [26]. Stage-specific genes were defined by the intersection of genes with stage effect in glia (padj < 0.01 and $|\log_2 FC| > 1$) and no interaction effect in either hemocytes or neurons (padj > 0.01 | $|\log_2 FC| < 1$). Dendrogram, principal component analysis (PCA), and Heatmaps were drawn using variance stabilization transformed data.

Gene Ontology (GO) analysis was performed using Pangea, DRSC—Harvard Medical School (https://www.flyrnai.org/tools/pangea/web/home/7227). Background for GO analysis was defined as the universe of detectable genes (counts > 0).

ATAC-seq

ATAC-seq was performed on L3 CNS from *rad50*$^{\Delta 5.1}$ or *w*^{1118} (control) animals in triplicates. Twenty CNS for each replicate were dissected on ice in PBS supplemented with 1% bovine serum albumin (BSA). Cells were extracted in 200 µl collagenase IV (Gibco ref: 17104019) at 1 mg/ml at 37°C for 30 min. To enhance dissociation, samples were pipetted 50 times every 10 min and 100 times at $t = 30$ min. Cells were counted on hemocytometer and 200 000 cells for each reaction were used. Upon dissociation, cells were centrifuged for 10 min at 600 × *g* and 4°C and nuclei were extracted in nuclei extraction buffer (HEPES, pH 8.0 20 mM, KCl 10 mM, Glycerol 20%, triton X-100 0.1%, spermidine trihydrochloride 0.5 mM) for 10 min on ice. Nuclei were pelleted at 1200 × *g* for 10 min at 4°C. Tagmentation was performed on extracted nuclei at 37°C for 30 min at 800 rpm in tagmentation buffer (Tris–HCl, pH 8 33 mM, N,N-Dimethylformamide (DMF) 16%, K-Ac 66 mM, $MgCl_2$ 10 mM, digitonin 0.001%, tween 20 0.01%, PBS 0.4×) using pre-indexed assembled Tn5 transposomes (Active Motif, ref 53152). DNA was recovered using MinElute purification kit (Qiagen ref: 28004). Libraries were prepared from the whole tagmented DNA using Q5® High-Fidelity 2X Master Mix (NEB) and P5/P7 primers at 1 µM final concentration in 50 µl total reaction volume and following polymerase chain reaction (PCR) program: 72°C 5 min/98°C 30 s/ (98°C 10 s, 63°C 30 s, 72°C 1 s) × 12 cycles. PCR clean-up was performed using SPRIselect size-selection beads (Beckman coulter) with a ratio of 1.2. Library quality was assessed on Agilent bioanalyzer using high-sensitivity chips. If adapters remained, those were removed with another size-selection step with 1.2 or 1.1 ratio according to amount and size of the contamination.

ATAC-seq analysis

Sequencing reads were trimmed using Trim Galore (paired-end mode, minimum length 25 bp, –trim1 option). Trimmed reads were aligned to the *Drosophila melanogaster* reference genome (dm6/BDGP6) [27] using Bowtie2 [28] with parameters: –very-sensitive-local, –dovetail, –no-unal, -I 25, -X 500, and –fr. Alignments were filtered for high-quality reads (mapping quality ≥10) and unmapped, secondary, and supplementary alignments were removed using samtools. Mitochondrial reads were quantified and removed. Peaks were called on individual samples using MACS2 [25, 25] (parameters: -f BAMPE, –gsize 120 000 000, –keep-dup = all, *P*-value cutoff 1e−5). FRiP scores were calculated using bedtools [29] intersect for quality control. Normalized bigWig files were generated using deepTools [30] bamCoverage. Alignment and peak calling stats are described in Supplementary Table S1. A consensus peak set of 26 996 regions was generated by merging all peaks detected across samples. Differential accessibility analysis was performed using DESeq2 [24, 25]. Peaks with $|\log_2 FC| > 1$ and adjusted *P*-value <.01 were defined as differentially accessible (Supplementary Table S7). Motif enrichment analysis was performed on differentially accessible peaks. Peaks were assigned as promoters [transcription start site (TSS)] if their center was located within 1500 bp upstream or downstream of a TSS; all other peaks were classified as enhancers. Genomic sequences were extracted using bedtools [29] getfasta from the *D. melanogaster* reference genome (dm6, r6.54). Upregulated peaks and downregulated peaks were analyzed separately using HOMER findMotifs.pl [31] with parameters: -len 8,10,12 (motif lengths), -S 25 (number of motifs to find). All peaks were used as background to control for sequence biases in accessible chromatin regions. Both *de novo* motif discovery and known motif enrichment were performed.

Histone extraction and western blot

Histones WB

Histones from E16 and L3 *w*^{1118} animals were extracted as described in Abcam histone extraction protocol (https://www.abcam.com/protocols/histone-extraction-protocol-for-western-blot) with minor modifications. Cells were extracted from three plates of 12–15 h aged embryos or 3 × 20 L3 larvae using Dounce homogenizer. Before extraction, larvae were open by pulling the cuticle on the ventral and dorsal side. Cells were isolated using Dounce homogenizer large and tight (50 strokes each) and cleared using a 50-µm filter. To remove remaining fat from larval samples, probes were centrifuged up to three times 10 min 4°C 600 *g*. Nuclei were extracted in extraction buffer [PBS 1×, Triton X-100 0.5%, PMSF 2 mM, NaN3 0.02%, Protease Inhibitor Complete (Roche) 1×] 10 min on ice, centrifuged at 1200 × *g* for 10 min at 4°C. Histones were extracted from nuclei in 1 ml of ice-cold HCl 0.4 N 10% glycerol overnight on a balancelle and precipitated by adding 8 volumes of ice cold acetone at 16 000 × *g* 30 min 4°C. Histone pellets were washed three times in 8 ml ice-cold acetone at 16 000 × *g* 30 min 4°C, dried at RT, and resuspend in 100 µl H_2O. Histone were quantified using Bradford reagent (Thermo Scientific ref: J61522-K2), equilibrated, and loaded on a 15% polyacrylamide gel. Upon electrophoresis, probes were transferred onto nitrocellulose membrane for 2 h at 300 mA on ice and revealed with mouse anti-γH2Av (1:500) (Developmental Studies Hybridoma Bank, AB_2618077) and rabbit anti-H3 (1:10 000) (Abcam ab1791). Signal was detected with Amersham ECL Select Western Blotting Detection Reagent using HRP-conjugated secondary antibodies (1:5000, Jackson, #111-035-045). Acquisition was performed on Amersham ImageQuant 800 imaging system with increasing exposure duration starting from 0.1 s until saturation. Quantification of blots was performed using Fiji gel analysis tool.

Rad50 WB

Western blots for Rad50 were performed on protein extract from 10 CNS per sample (*w*^{1118} or *rad50*$^{\Delta 5.1}$) per replicate. For protein extraction, CNS were dissected in PBS, crushed using a microtube pestle in 50 µl lysis buffer [Triton X-100 0.1%, NaCl 150 mM, tris 50 mM, $MgCl_2$ 5 mM, 0.5 mM PMSF, protease inhibitor cocktail (Roche)], incubated on ice 30′ with mixing every 10′, and centrifuged at 10 000 × *g* for 10 min at 4°C. The supernatant was recovered and heated after adding 1V of Laemmli 2× containing 200 mM freshly added DL-Dithiothreitol (DTT) at 95°C for 5 min. Protein extracts were separated by 8% sodium dodecyl sulfate–polyacrylamide gel electrophoresis, transferred onto nitrocellulose membrane 1 h 30 min at 200 mA on ice and probed for Rad50 (1:10 000) or actine (1:1000). Signal was

detected with Amersham ECL Select Western Blotting Detection using HRP-conjugated secondary antibodies (1:5000, Jackson, #111-035-045).

Immunolabeling of polytene chromosomes

Salivary glands were dissected from L3 larvae in NaCl 0.7% NP-40 0.1% and fixed for 2 min in 3.7% formaldehyde 0.7% NaCl 1% Triton-X. Before squashing, the glands were transferred in 2% formaldehyde 45% acetic acid and incubated for 2 min on a siliconized coverslip. During incubation, salivary glands were fragmented. A poly-L-lysine slide was inverted on top of the coverslip and salivary glands were squashed. The chromosome spreads were examined by phase microscopy and frozen in liquid nitrogen. The coverslip was flicked off with a razor blade and slides were incubated in cold PBS 2× for 15 min. The slides were transferred to a blocking solution (3% BSA, 2% NP-40, 0.2% Tween 20, 10% nonfat dry milk in PBS) and blocked for 1 h at RT. After blocking, slides were incubated with primary antibody in blocking solution overnight at 4°C in a humid chamber. Slides were then rinsed in PBS and washed 2× 15 min in PBS 1×/0.2% Tween/0.1% NP-40. After washing, slides were rinsed in PBS and incubated with secondary antibody in blocking solution for 2 h at RT in a humid chamber. Slides were then rinsed in PBS and washed 2× 15 min in PBS 1×/0.2% Tween/0.1% NP-40. Finally, slides were drained and mounted with Vectashield medium H-1200 with DAPI to stain DNA. The primary antibodies used for immunolabeling were rabbit anti-H3K4me3 1:400 (Abcam ab8580); mouse anti-H3K9me2 1:20 (Abcam ab1220); rabbit anti-H3K9me3 1:100 (Abcam ab8898); rabbit anti-H3K27me3 1:400 (Cell Signaling C36B11); mouse anti-γH2Av 1:20 (DSHB AB_2 618 077); and rabbit anti-Rad50 1:100 (custom-made by Agrobio [15]). The secondary antibodies were: FITC-conjugated goat anti-rabbit 1:50 (Jackson) and Rhodamine-conjugated goat anti-mouse 1:50 (Jackson). Polytene chromosomes preparations were analyzed on a fluorescence microscope (Zeiss Apotome) and images acquisition performed using the Zen Pro software (Zeiss). Polytene chromosome fluorescence intensity and bands plot profile analysis were performed using Fiji software (National Institute of Mental Health, Bethesda, Maryland, USA). Welch *t*-test was used to compare polytene chromosome intensities between *rad50* KO and control.

CNS squash

Welch *t*-test was used to compare histone mark intensities between *rad50* KO and control. Outliers were removed if cell-signal >2× IQR resulting in 5.01% of cells removed for H3K4me3 and 2.85% of cells removed for H3K27me3.

LC–MS/MS

Proteomic analysis was performed at the Proteomics facility from IBMC Strasbourg with the help of Philippe Hamman and Johana Chicher.

Liquid chromatography assay coupled to tandem mass spectrometry (LC–MS/MS) analysis of Rad50 co-immunoprecipitation (co-IP) was performed on dissected CNS from w^{1118} or $rad50^{\Delta 5.1}$ (control) L3 larvae in three replicates, 100 CNS per replicate. Upon dissection, brains were snap frozen in liquid nitrogen and stored at −80°C until protein extraction. Brains samples were squashed with 10 strokes of microtube pestle in extraction buffer [Triton X-100 1%, NaCl 50 mM, tris 50 mM, $MgCl_2$ 5 mM, 0.5 mM PMSF, Protease Inhibitor Complete (Roche)]. Samples were incubated for 30 min on ice, mixed every 10 min. IP was performed on 250 µg total protein extract using Miltenyi Protein-A beads and 5 µl antibody for each IP. Mass-spectrometry was performed on TIMS-TOF Pro2 mass spectrometer. Label-free quantification was applied and proteins were then selected based on fold change and *P*-value as indicated in figure descriptions. Two thousand nine hundred fifteen proteins were identified in total. Proteins without valid peptide detection were removed (2570 remaining), proteins from known contaminants based on cellular localization ("mitochondrion," "endoplasmic reticulum," "golgi," "clathrin," "peroxisomal," "mitochondrial," "endosome," "endoplasmic," "secreted," "endomembrane") were removed (2077 remaining). Finally, 260 significant (padj < 0.01) enriched ($log_2FC > 1$) interactants were kept. Reactome enrichment analysis was performed on the detected interactants on string-db.org.

RT-qPCR

RNA was extracted from crushed L3 larvae or E16 w^{1118} embryos using TRI reagent following the manufacturers' protocol. For Real-time quantitative PCR (RT-qPCR) on larval CNS, 10 dissected CNS per sample were used. RNA quality was assessed by Nanodrop and samples were equilibrated to 250 ng/µl. Reverse transcription (RT) was performed on 500 ng of total RNA using LunaScript® RT SuperMix Kit (NEB). A no-RT control was included to test for genomic DNA (gDNA) contamination. qPCR was performed on 2 µl of complementary DNA (cDNA) diluted 1/5 using Roche SYBR green I Master mix on a Roche Lightcycler 480 using standard protocol. No-cDNA control was included for primer-dimer background estimation. Each of the three biological replicates was run as three independent technical replicates, each measured in duplicate. We first averaged the two Ct-duplicates for each technical replicate. For any technical replicate, if the two duplicate Ct values had a standard deviation greater than 0.5 and the standard deviation across the three technical replicates for that biological replicate was >1, that measurement was excluded. Relative gene expression was calculated using the $2^{-\Delta Cq}$ method, normalizing to the geometric mean of two housekeeping genes (Rp49 and Act5C). If one of the housekeeping was not detected, that sample was removed. Statistical significance was assessed using paired *t*-tests on relative expression values (mean of up to three measurements per biological replicates) to account for batch effects from day-to-day processing variation. Error bars represent the standard error of the mean (SEM) of log_2-fold changes across biological replicates. Primers used for RT-qPCR are listed in Supplementary Table S3.

Immunolabeling and RNA *in situ* hybridization

In situ hybridization

In situ hybridization was performed using the HCR™ RNA-FISH kit from Molecular Instruments on 10 larval CNS per sample following the manufacturer's guidelines with minor modifications.

Immunolabeling

Dissected CNS (10 per replicate) were fixed for 20 min at RT in 4% PFA, washed three times for 10 min with PTX

(PBS + Triton X-100 0.1%), blocked with blocking reagent for 2 h, and incubated with primary antibodies overnight [rat anti-Dpn, Abcam #ab195173, 1/500; mouse anti-pH3, Millipore #05-806 (3H10), 1/200; rabbit anti-Dcp1, Cell Signaling #9578S, 1/500]. CNS were then washed three times with PTX for 10 min on a rocker, incubated for 2 h at RT with secondary antibodies (1/500), washed three times in PTX for 10 min at RT on a rocker, incubated for 30 min with DAPI (1/5000) at RT on a rocker, washed once in PTX, and mounted in Vectashield.

Image acquisition and analysis

Image acquisition was performed on a Leica SP8 confocal microscope. Cells were counted using the Spots detection module in Imaris (version 11.0, Oxford Instruments). Z-stack confocal images were imported and the Spots function was used to automatically detect positive cells based on fluorescence. Cell diameter was assessed by averaging cell measurements for each marker, and background subtraction was enabled. Detection thresholds were manually adjusted to minimize false positives and negatives, and results were visually verified on each image. Total cell counts were exported per CNS for statistical analysis. Images for figures were processed using Fiji.

Extended bioinformatic analysis

Bioinformatic analyses were performed using R studio version 4.1.0 (2021-05-18), RStudio Team (2021). RStudio: Integrated Development Environment for R. RStudio, PBC, Boston, MA, URL http://www.rstudio.com/. Multiple packages were used: dplyr version 1.0.6, ggplot2 version 3.4.2, gdata version 2.18.0, tidyr version 1.1.3, ggpubr version 0.4.0, corrplot version 0.90, ggrepel version 0.9.1, DESeq2 [25, 25] version 1.32.0, R Core Team (2021). R: A language and environment for statistical computing. R Foundation for Statistical Computing, Vienna, Austria. https://www.R-project.org/.

Database and tools

Flybase [32]. Flyprimerbank [33] was used to design qPCR primers. IGV [34] was used for visualization purposes.

Results

Developmental stage is the main feature of cell identity

We recently characterized the cell-type-specific transcriptional signatures in *Drosophila* glia, hemocytes, and neurons from E16 and L3 stages [5]. Using the same RNA-seq dataset (Supplementary Table S1), we performed a comparative E16 versus L3 analysis across the three cell types to assess the contribution of developmental stage to transcriptional identity. While genome-wide analyses suggest that temporal signatures play a significant role, this issue remains poorly understood [35, 36].

To extract the most important features from our dataset, we applied a PCA (Fig. 1A). This analysis revealed developmental stage as the dominant source of variation: principal component 1 (PC1) (65.9% of total variance explained) separates embryonic (E16) from larval (L3) samples, while PC2 (22.4% of variance) captures cell-type differences (Fig. 1A). We then confirmed this dominant stage effect by computing hierarchical clustering of Euclidean distances (HC) (Fig. 1B). HC clustering aims to identify similarities between samples by comparing their overall gene expression profiles. This analysis corroborates our conclusion from PCA, grouping the E16 and L3 samples into separate branches (Fig. 1B). We also noted that the distance between hemocytes, glia and neurons increases at L3 compared to E16 suggesting greater similarities between the cell-types at embryonic stage compared to larval stage (Fig. 1A and B).

Together, these results robustly demonstrate that developmental stage, more than cell type, is the dominant driver of variability in our dataset.

Stage-specific transcriptional features in embryonic and larval cells

To capture stage-specific features common to all three cell types, we examined which genes show consistent expression changes from E16 to L3 in neurons, glia, and hemocytes. We fitted a DESeq2 model incorporating cell-type, developmental stage, and their interaction (~ cell-type + stage + cell-type:stage). This interaction model identifies stage effects and tests whether they are consistent across cell types [24, 25, 37]. We selected genes with significant stage effect ($|\log_2 FC| > 1$, padj < 0.01) and no statistically detectable interaction ($|\log_2 FC| < 1$ or padj > 0.01), yielding 2533 stage-specific genes. Clustering these genes by their z-scored expression divides them into those enriched at E16 versus L3 stage, confirming the effectiveness of our gene-selection pipeline (Fig. 1C and Supplementary Table S2).

To identify key biological processes enriched in the stage-specific gene pool, we next performed a GO analysis [38–40]. E16-upregulated genes are enriched for only one statistically significant term, "cuticle development," in line with larval cuticle formation occurring at this stage [41–43]. On the other hand, L3-upregulated genes show a strong enrichment for "DNA repair" along with "chromatin organization" and metabolic processes (Fig. 1D). In sum, we detected 2533 stage-specific genes, with 1833 upregulated at E16 and 700 at L3. Hence, despite comprising the larger gene set, E16-specific genes display limited functional convergence, while the smaller L3-specific gene set shows strong enrichment for shared biological processes including DNA repair and chromatin organization.

To further investigate these findings and test whether the enrichment of DNA repair genes is a global, cell-type-independent stage feature, we compared whole animals at E16 and L3 stage. We selected from the literature the most important genes involved in the main DNA repair pathways and compared their expression levels in whole animals at E16 and L3, using RT-qPCR assays (Supplementary Fig. S1A and Supplementary Tables S3 and S4) [15, 44–46]. Out of the 26 tested genes, 19 (73%) are significantly overexpressed at larval stage, including major DNA repair complexes such as the double strand DNA break (DSB) repair complex MRN (Mre11, Rad50) involved in homologous recombination [15, 16] and key components of the nonhomologous end joining (NHEJ) repair complex like *ku80* and *irbp/ku70* [45, 47] (Supplementary Fig. S1A). To compare our RT-qPCR results to the transcriptomic dataset, we pooled all RNA-seq samples together by stage and applied DESseq2 differential expression analysis, allowing us to extract E16/L3 fold change values. RNA-seq and RT-qPCR analyses display a strong linear correlation ($R = 0.75, P = 3.4e{-}05$) further validating our results and reinforcing DNA repair as an L3-enriched feature (Supplementary Fig. S1B).

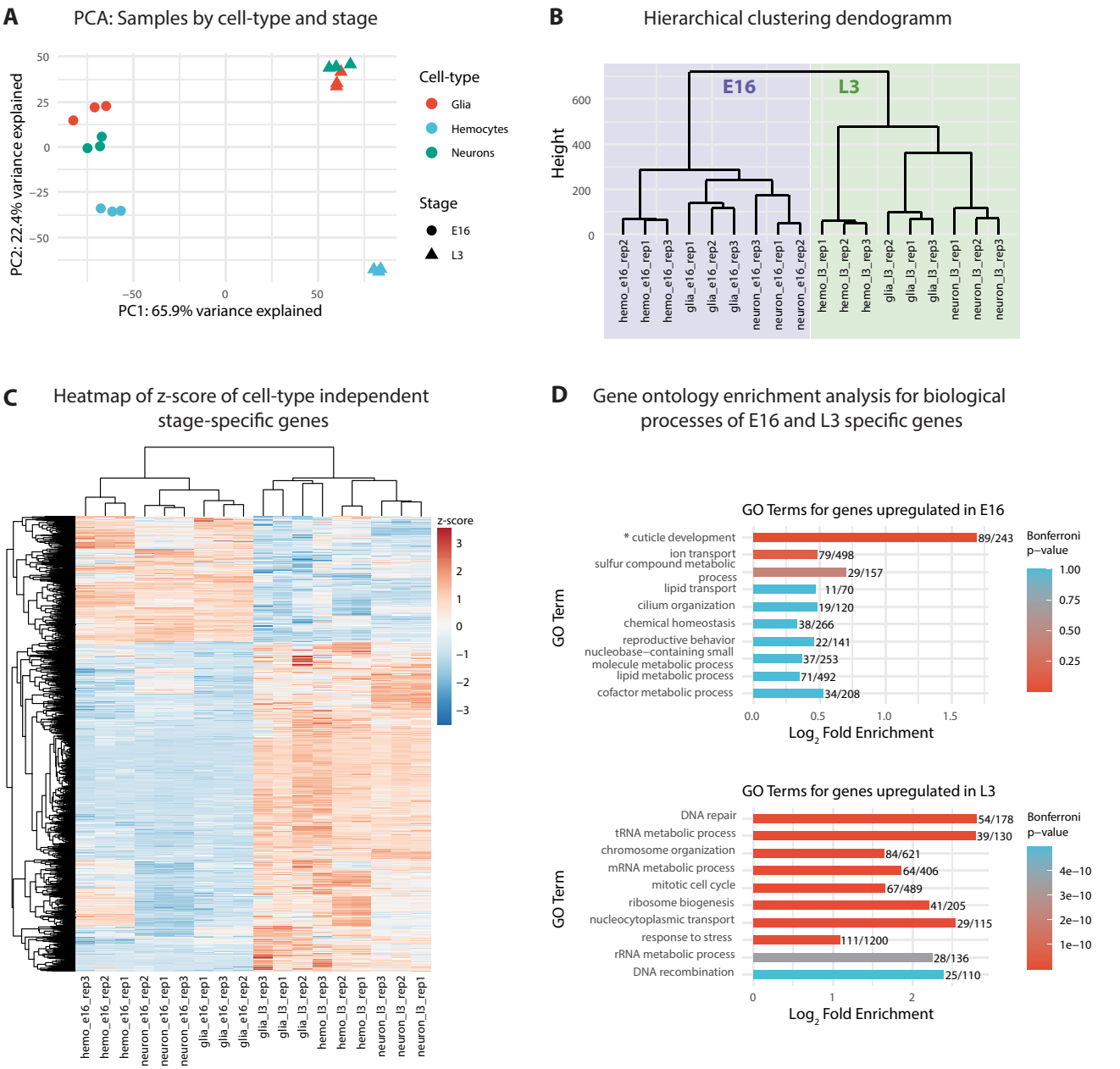

Figure 1. A) PCA of RNA-seq assays in E16 and L3 glia, hemocytes, and neurons. PC1 and PC2 are shown. (**B**) Hierarchical clustering of Euclidean distances of RNA-seq assay. (**C**) Heatmap of *z*-scores of cell-type-independent stage-specific gene expression. Each raw represents a gene. Hierarchical clustering in rows and columns shown. (**D**) GO analysis of biological processes for E16 ((**C**) top, 1833 genes) or L3 ((C) bottom, 700 genes) stage-specific genes. Top 10 terms are shown. ∗ Cuticle development is the only significant term in E16 enriched genes.

In sum, the transcriptomic assay reveals developmental stage as a main feature of cell identity. We identify cuticle development and DNA repair as stage-specific features of E16 and L3 stage, respectively. The L3-specific genes show stronger functional convergence than the embryonic-specific genes, consistent with each cell type primarily executing its own lineage specification and differentiation programs at this stage.

Rad50 interacts with a broad spectrum of chromatin associated proteins

The coordinated transcriptional change across multiple DNA repair pathways and cell types raises interesting questions about the role of these genes at the larval stage. Given the consistent upregulation of the MRN complex members Rad50 and Mre11 at the larval stage, we chose to further investigate Rad50 to understand its potential functions in this developmental context.

We first asked whether the upregulation of the DNA repair pathways and especially of the MRN complex correlates with increased DNA damage and measured gammaH2Av (γH2Av), a hallmark of DSB [48], via western blot in whole E16 and L3 animals. γH2Av levels are not higher at larval compared to embryonic stage (Fig. 2A). We next complemented those data by analyzing the colocalization of Rad50 and γH2Av in polytene chromosomes extracted from larval salivary glands using immunolabeling (Fig. 2B). Polytene chromosomes are

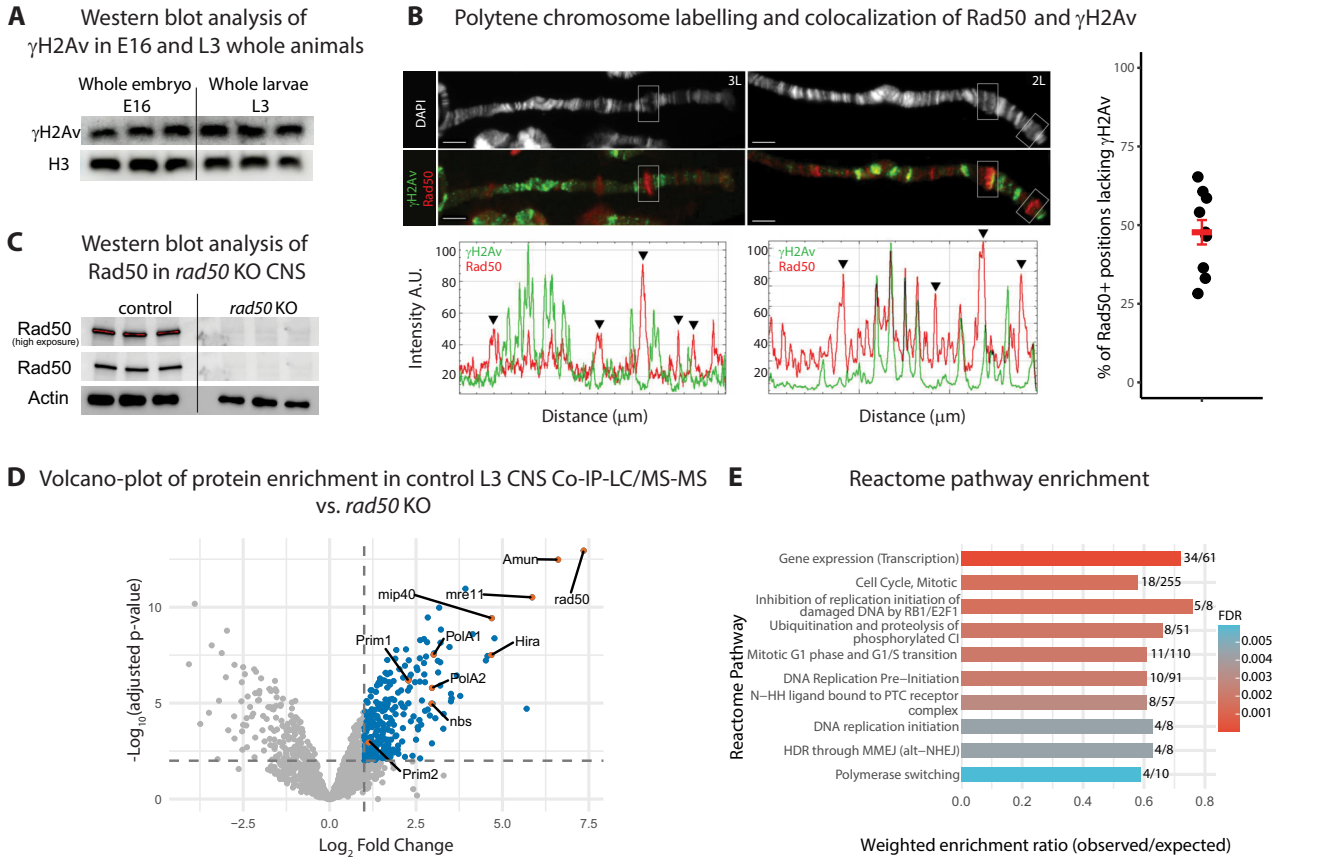

Figure 2. (**A**) Western blot analysis of the DNA double strand mark γH2Av in E16 and L3 samples. $n = 3$, One representative replicate shown. (**B**) Left, Polytene chromosome labeling for Rad50 and γH2Av. Right, Percentage of Rad50 binding positions lacking γH2Av. (**C**) Western blot analysis of Rad50 expression levels in control and *rad50* KO CNS. (**D**) Volcano plot of LC–MS/MS results in L3 CNS control versus *rad50* KO. In blue: significant interactants (padj < 0.01 and $\log_2$(Fold change) > 1. In red: Genes of interest. (**E**) Reactome pathway enrichment analysis for significant interactants detected in the Co-IP-LC-MS/MS of Rad50.

characterized by the alternation of dense (heterochromatic, H3K9me3 positive) and less dense (euchromatic, H3K4me3 positive) bands, a reflection of the chromatin condensation state and gene activation [49]. They have been widely used to study the distribution and colocalization of chromatin-associated proteins including DNA-repair proteins but also proteins and transcription factors linked to chromatin organization [15, 16, 49–51].

Quantification of Rad50 peaks distribution along polytene chromosomes arms revealed that 47.7% of Rad50-positive peaks occur in regions lacking detectable γH2Av, indicating that a substantial fraction of Rad50 recruitment takes place outside γH2Av—marked chromatin (Fig. 2B, black arrows). These results suggest that Rad50 binding to chromatin is not solely driven by DNA damage and γH2Av, in line with recent studies pointing to broader chromatin-associated roles [20, 21].

The above data suggest that the coordinated upregulation of DNA repair genes at L3 is not driven by increased DNA damage, prompting us to investigate other possible roles for these factors. To identify partners that could explain Rad50 presence in the absence of DNA damage, we conducted an LC–MS/MS analysis of Rad50 co-IP in larval CNS dissected from control or *rad50* null mutant animals (*w;rad50*$^{\Delta 5.1}$*;+* also called knock-out or KO) as a control. We used larval CNS as a proxy for late larval stage because it provides a more homogeneous, yet sufficiently complex system compared to whole larvae, simplifying both technical execution and analytical interpretation. Successful depletion of Rad50 in the KO samples was confirmed by western blot (Fig. 2C). Out of 2915 detected proteins, we identified 260 specific interactants based on stringent criteria ($\log_2$FC > 1, padj < 0.01). We detected Rad50 as first hit as well as MRN complex components Mre11 and Nbs among the top hits, in agreement with published data and validating our approach (Fig. 2D and Supplementary Table S5) [15, 16]. Rad50 was not detected in the KO (Supplementary Table S5).

Interestingly, we also detected robust interactions with the complete alpha-primase polymerase complex (PolA1, PolA2, Prim1, Prim2), essential for DNA replication initiation via RNA primer synthesis (Fig. 2D) [52, 53]. Although DNA replication is a source of DNA damage and the stability of the replication fork is a crucial determinant of genome integrity, a direct interaction between alpha-primase polymerase and Rad50 had not been previously demonstrated. Our results suggest that Rad50 may associate with replication machinery, possibly assisting in maintaining genomic stability during DNA replication and cell division and in prevention or repair of collapsing replication forks [54, 55]. Direct interaction between Mre11 and stalled replication forks has already been documented in mouse embryonic fibroblasts and yeast [56, 57].

Among novel significant interactants, we identified Amun, Hira, and Mip40 (Fig. 2D). Amun is a genetic repressor of Notch signaling involved in stem cell maintenance in the gut [58, 59]. Hira is a histone chaperone involved in nucleosome assembly during zygotic genome activation, fertilization, and in transcription related histone deposition in *Drosophila* [60–62]. In mammals, Hira is involved in transcriptional regulation and DNA repair [63, 64]. Mip40 is a member of the Myb–MuvB transcriptional activation complex, regulating G2/M phase gene expression [65, 66]. Finally, pathway enrichment analysis using Reactome [67], a curated and peer-reviewed database for proteomics, underscored interactions relevant to gene expression regulation, DNA repair, and cell-cycle-associated processes, suggesting involvement in multiple aspects of genome regulation (Fig. 2E).

Altogether, and in line with recent findings in other systems, our data suggest possible links between Rad50, DNA replication, and genome regulation in *Drosophila* larvae, in addition to its established role in DNA repair [20, 21, 68].

Histone modification patterns are altered in *rad50* KO polytene chromosomes

The diversity of the interactants, related to DNA-repair as well as gene expression, goes along with studies reporting DNA repair machineries to be interlinked with genome regulation and gene expression. The MRX complex has been reported to function as a chromatin insulator and to regulate gene expression in yeast [21]. MRE11/NBS1 in mammalian cells colocalize with RNA polymerase II at active genes, limiting transcription-associated damage and affecting polymerase dynamics [69]. Also, Ku proteins involved in NHEJ have been shown to function as transcription factors [70–72]. Histones, which regulate chromatin structure and gene expression while serving as platforms for critical modifications, are tightly linked to DNA repair processes, with γH2A being the most prominent example [48]. More broadly, histone modifications undergo dynamic transitions during DNA repair. For instance, loss of repressive marks such as H3K9me3 followed by chromatin relocation accompanies DNA repair processes of damages located in heterochromatin in *Drosophila* [73]. Similarly, histone hyperacetylation promotes DNA repair and histone chaperones are essential for nucleosome reassembly following repair [74–78].

In *Drosophila*, Rad50 is known to associate to histone mark H3K9me3 and to HP1, two hallmarks of repressed chromatin [19]. To determine whether Rad50 has an impact on chromatin regulation in *Drosophila*, we tested whether its absence leads to changes in chromatin structure upon polytene chromosome labeling of histone modifications associated to eu- or heterochromatin. We analyzed three marks representing distinct chromatin states: H3K4me3, for active promoters and euchromatin; H3K9me2/3, for constitutive heterochromatin at telomeres and centromeres; and H3K27me3 for Polycomb-mediated facultative heterochromatin associated to transcriptional repression [79–81].

Quantitative analyses of polytene chromosomes show significant increase in H3K4me3 and decrease in H3K9me2/3 signals in *rad50* KO compared to control (Fig. 3A). At a refined scale, the distribution of H3K4me3, and thus of euchromatin, appears to be modified when comparing KO to control, which might indicate that new sites have become active (Fig. 3B, black arrows). This is accompanied by a strong decrease of the repressive mark H3K9me3 that can be observed on the telomere regions (Fig. 3C and Supplementary Fig. S2). By contrast, H3K27me3 levels increase significantly in *rad50* KO polytene chromosomes (Fig. 3D and E). We then tested whether lack of Rad50 leads to increased DNA damage and observed significant enrichment of γH2A (Fig. 3D and E). Having identified chromatin-associated proteins as Rad50 interactants through mass spectrometry in larval CNS (Fig. 2D), we examined whether histone modifications are affected in this tissue as well and found increased H3K4me3 and H3K27me3 signals in *rad50* KO CNS larval squashes compared to control (Fig. 3F).

In sum, immunolabeling of polytene chromosomes reveals significant alterations in histone mark levels and distribution in *rad50* KO: increased H3K4me3 with altered chromosomal distribution, decreased H3K9me2/3, and increased H3K27me3. These reciprocal changes in repressive marks—decreased H3K9me2/3 versus increased H3K27me3—show that Rad50 loss results in a disrupted balance between different chromatin states rather than simply opening or closing chromatin. Crosstalk between histone marks has also been widely described: while the two repressive marks H3K9me2/3 and H3K27me3 are exclusive in normal conditions and are partitioned into separate chromatin compartments, a mutation of the H3K9me2/3 depositing enzyme SUV3-9H1/H2 leads to ectopic gain of H3K27me3 at pericentric heterochromatin [79, 82, 83]. Similar observations have been reported at pericentric heterochromatin in 2i-ESCs [84]. This plasticity in repressive chromatin states implies that breaking the normal partitioning of histone marks can reshape the broader chromatin landscape. While some of these effects we observe here may be indirect given the constitutive absence of Rad50, the range of histone mark changes on polytene chromosomes, combined with its diverse interactants (Fig. 2), suggest that Rad50 may contribute to maintaining the balance between chromatin states in addition to its canonical role in DNA repair.

Transcriptome changes in *rad50* KO CNS

To assess whether the chromatin alterations observed upon Rad50 loss are associated with changes in gene expression, we performed an RNA-seq assay on CNS from control and *rad50* KO larvae (Supplementary Tables S1 and S6).

Differential expression analysis of RNA-seq identified 1420 genes significantly affected by Rad50 loss ($|\log_2 FC| > 1$, padj < 0.01), with 1058 being upregulated and 362 downregulated (Fig. 4A). The predominance of upregulated genes (74.5% out of total DEG) is consistent with our observation of decreased H3K9me2/3 repressive marks and increased H3K4me3 activating mark in *rad50* KO polytene chromosome (Fig. 3A and Supplementary Fig. S2).

GO analysis revealed distinct functional signatures: downregulated genes are enriched for terms related to cell differentiation, development, and gene expression regulation (Fig. 4B). The genes upregulated in the KO show enrichment for stress response pathways (Fig. 4B), see GO terms “immune response” and “sulfur compound metabolic process” (includes glutathione signaling terms). Interestingly, we found genes related to cuticle development, a term specifically enriched at E16, being upregulated in *rad50* KO larval CNS (Fig. 4B and C).

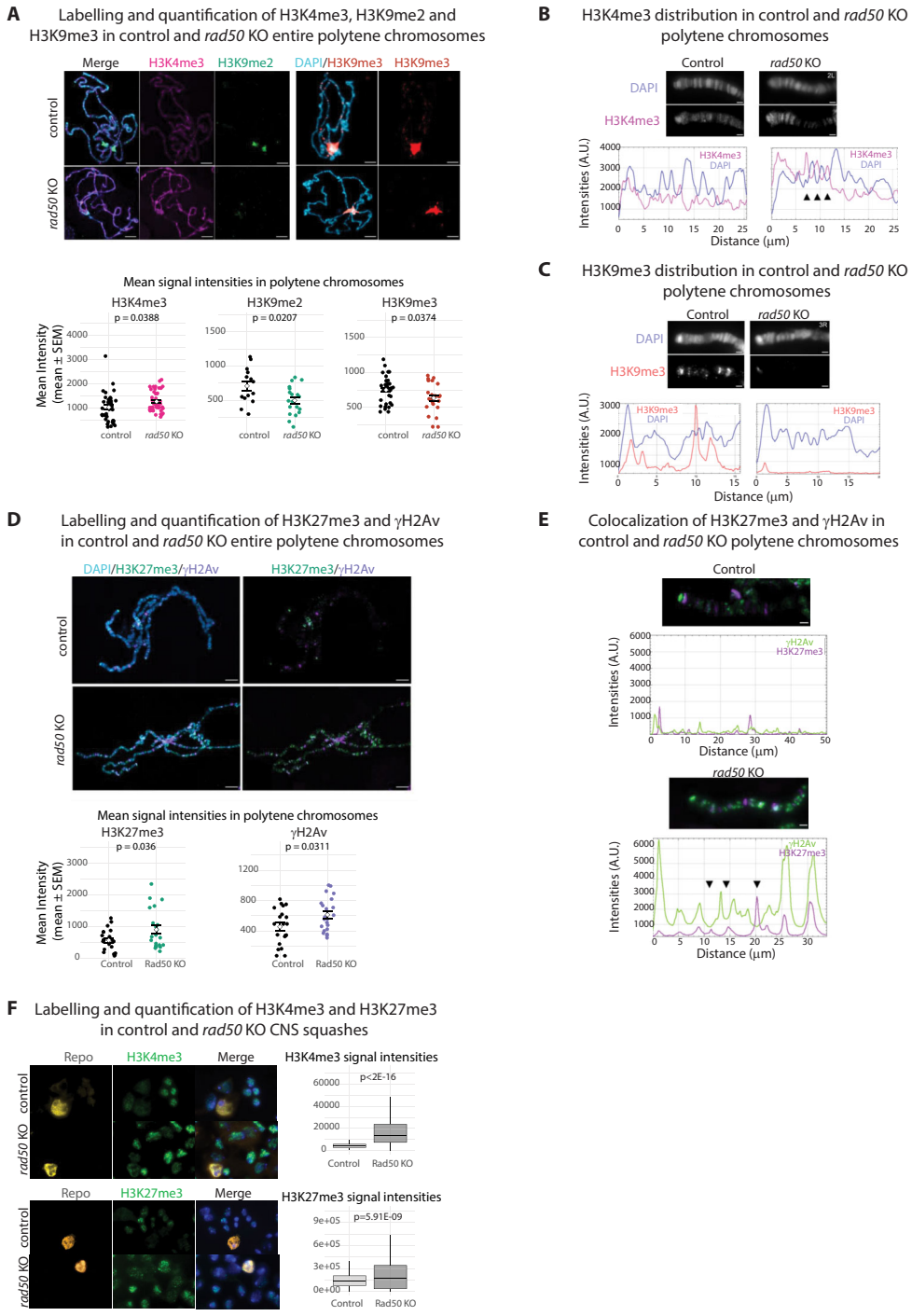

Figure 3. (**A**) Top, Representative polytene chromosomes immunolabeled with anti-H3K4me3 (magenta) and anti-H3K9me2 (green), or with anti-H3K9me3 (red), from control or *rad50* KO homozygous mutants L3. Chromosomes were counter-stained with DAPI (blue). Scale bar = 20 µm. Bottom, Fluorescence intensity quantification of polytene chromosomes of the heterochromatic marks H3K9me2 H3K9me3, in *rad50* KO compared to control. Each dot represents a single polytene chromosome ($n \geq 13$). Arbitrary unit (A.U.). Error bars represent SEM. Welch parametric *t*-test. (**B**) Representative intensity profiles of H3K4me3 and DAPI signals over a segment at the tip of chromosome 2L, showing an alteration of the H3K4me3 signal in *rad50* KO compared to the control; arrowheads denote regions of strong difference of H3K4me3 in *rad50* KO compared to control. *y*-axis: fluorescence intensity; *x*-axis: distance from the tip of the chromosome (µm). Scale bar = 10 µm. (**C**) Representative intensity profiles of H3K9me3 and DAPI signals over a segment at the tip of chromosomes 3R showing the absence of H3K9me3 signal in *rad50* KO compared to control. *y*-axis: fluorescence intensity; *x*-axis: distance from the tip of the chromosome (µm). Scale bar = 10 µm. (**D**) Top, Representative polytene chromosomes immunolabeled with anti-H3K27me3 (purple) and anti-γH2Av (green), from control or *rad50* KO larvae. Chromosomes were counter-stained with DAPI (blue). Scale bar = 20 µm. Bottom, Fluorescence intensity quantification showing increase of both H3k27me3 and γH2Av signals in *rad50* KO compared to control. Each dot represents a single polytene chromosome ($n \geq 15$). Error bars represent SEM. Welch parametric *t*-test. (**E**) Representative intensity profiles of H3K27me3 and γH2Av signals over a segment at the tip of the 2R chromosome. Note that the increase of γH2Av peaks in the *rad50* KO is not directly correlated with that of H3K27me3 (arrowhead). *y*-axis: fluorescence intensity; *x*-axis: distance from the tip of the chromosome (µm). Scale bar = 10 µm. (**F**) Repo, H3K4me3, and H3K27me3 labeling in isolated cells from squashed CNS. Quantification is shown on the right. Welch parametric *t*-test. Each experiment was performed on at least three brains (three biological replicates). Number of cells >370.

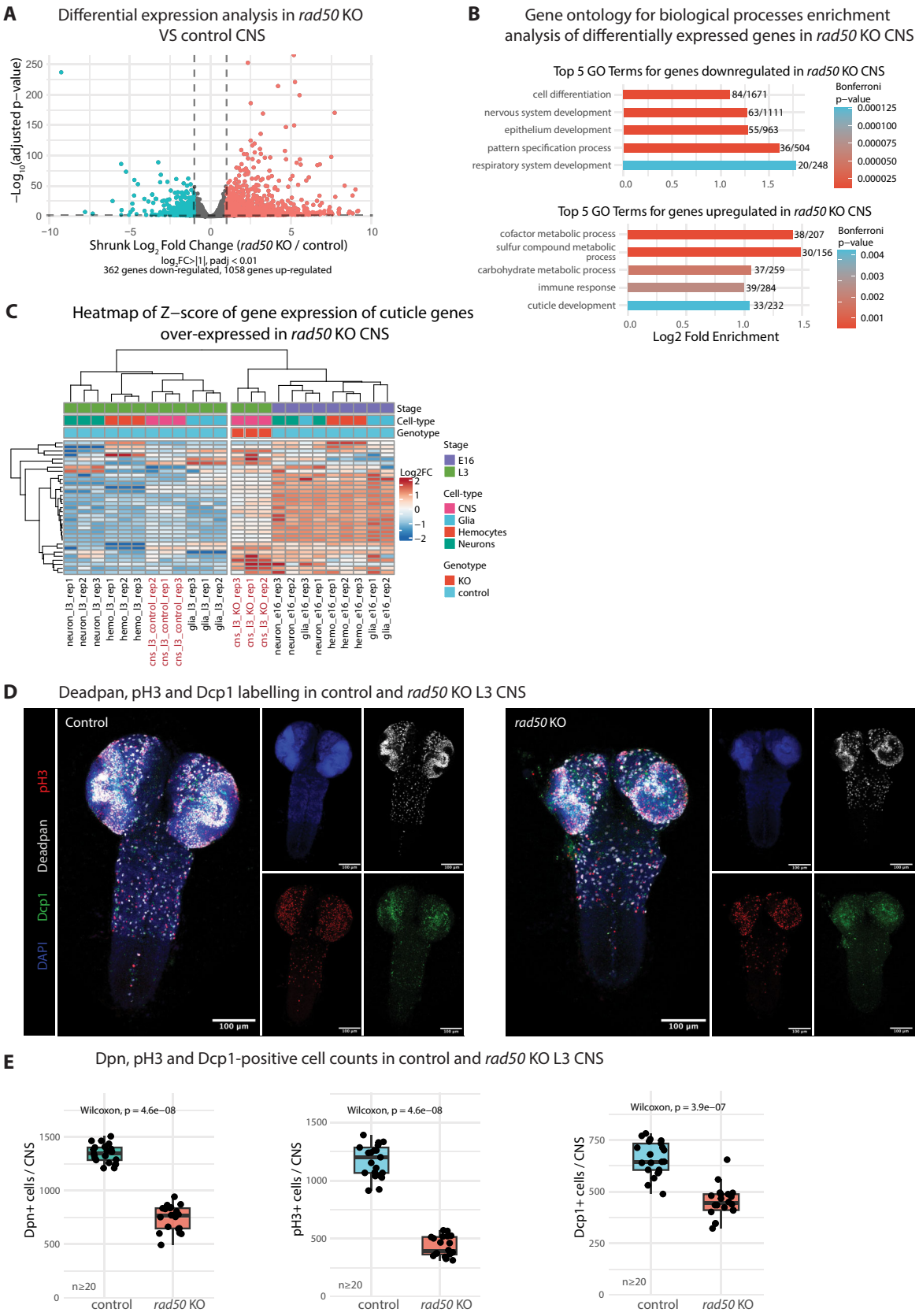

Figure 4. (**A**) Volcano plot of differential mRNA expression analysis in *rad50* KO versus control CNS. In red, genes enriched in KO CNS and in blue, genes enriched in control CNS. (**B**) GO analysis of biological processes for genes downregulated (top) or upregulated (bottom) in *rad50* KO CNS. Top 5 is shown. (**C**) Heatmap of cuticle gene expression enriched in *rad50* KO CNS versus control. Thirty three cuticle genes from "cuticle development" GO term, Fig. 4B shown. Hierarchical clustering in columns and clustering by correlation in row. (**D**) Phosphorylated histone 3 (pH3), Deadpan (Dpn), and Death caspase protein-1 (Dcp1) labeling in control and *rad50* KO CNS. $n > 20$, Wilcoxon test. (**E**) Dcp1, Dpn, and pH3-positive cell counting in control and *rad50* KO L3 CNS. Wilkoxon test, $n \geq 20$.

To assess whether these transcriptional changes were accompanied by cellular defects, we performed immunofluorescence assays on *rad50* KO larval CNS. The number of pH3-positive cells was reduced, indicating decreased mitotic activity (Fig. 4D and E). As the number of Dcp1-positive cells was also decreased, this reduction was not due to elevated apoptosis but rather reflects a global decrease in proliferation. Strikingly, the number of Deadpan-positive neuroblasts was also reduced (Fig. 4D and E), suggesting that Rad50 loss affects CNS development.

In sum, the transcriptomic and the *in vivo* analyses of larval CNS lacking Rad50 reveal global changes in gene expression.

Chromatin accessibility changes in *rad50* KO CNS

Given the observed changes in histone modifications and gene expression, we next asked whether Rad50 loss affects chromatin accessibility at a genome-wide scale and performed an ATAC-seq assay on CNS from control and *rad50* KO larvae in triplicate (for ATAC-seq metrics, sequencing statistics and analyzed data, see Supplementary Tables S1 and S7). Examination of signal enrichment patterns revealed that TSSs exhibit a global increase in accessibility in *rad50* KO samples (Supplementary Fig. S3A). This increased TSS accessibility is consistent with the predominance of upregulated genes (RNA-seq analysis; Fig. 4A), together indicating that Rad50 loss leads to a chromatin state more permissive for transcription.

To assess for accessibility changes between KO and control animals, we created a consensus peak set by merging all peaks identified across individual replicates using relaxed MACS2 [85] thresholds ($P < .05$), yielding 26 996 total regions (Supplementary Table S7). Reproducibility between our samples at consensus peaks was good as confirmed by Spearman correlation analysis (Supplementary Fig. S3B). Using the consensus peak set, we performed a differential accessibility analysis using DESeq2 [24, 25] and identified 1772 significantly affected peaks ($|\log_2 FC| > 1$, padj < 0.01), with 1170 regions showing increased accessibility and 602 showing decreased accessibility in *rad50* KO, with 24.8% of the peaks mapping to TSS (distance to TSS $\leq \pm 1500$ bp) and 75.2% to distal regulating elements or enhancers (Fig. 5A and Supplementary Fig. S3C). This bias toward increased accessibility further aligns with elevated TSS accessibility and the predominance of upregulated genes in the RNA-seq assay (Figs 4A, 5A, and Supplementary Fig. S3A).

To identify regulatory regions, we performed *de novo* motif discovery using HOMER on regions up or downregulated in *rad50* KO, respectively, 1170 and 602 regions. Among the upregulated sequences, we identified enrichment for GATA-factors motifs and for binding sites of two identified transcription factors: Zelda (Zld), Grainyhead (Grh) (Fig. 5B).

Zelda is a pioneer factor primarily known for its essential role in embryonic genome activation [86–89], but it also functions in larval Type II neuroblasts where it maintains stemness in synergy with Notch signaling [90, 91]. In the embryo, Zelda binding is strongly sequence-driven by its canonical motif, and embryo-specific ChIP-seq peaks are highly enriched for this motif. In larval brains, by contrast, Zelda-bound regions lack the canonical motif entirely and instead, Zelda binding correlates with pre-existing chromatin accessibility at promoters enriched for other motifs (Dref, GAF, M1BP). The canonical Zelda consensus is therefore a signature of embryonic, rather than larval, Zelda binding sites. The fact that our *de novo* motif analysis identifies this consensus in regions gaining accessibility in *rad50* KO (Fig. 5B) suggests that these regions correspond to embryonic Zelda regulatory elements.

Grainyhead is expressed in postembryonic neuroblasts where it regulates neural stem cell proliferation and Hox-dependent apoptosis [92–95]. Most importantly, Grh is also a master regulator of cuticular protein genes—the same gene class we identified as an E16 stage-specific signature as well as enriched in *rad50* KO CNS (Figs 1D and 4B and C) [43, 96–98]. Accordingly, *rad50* KO CNS show increased accessibility at *dsx-c73A*, a secreted cuticle protein, and other cuticle gene regulators including *gsb* and *dpy* (Fig. 5C–E). RT-qPCR analysis confirmed that both *zld* and *grh* are significantly upregulated in *rad50* KO larval CNS (Supplementary Fig. S3E), indicating that the motif enrichment is accompanied by elevated expression of these transcription factors. Interestingly, Zld and Grh compete for occupancy at embryonic enhancers during early development, where Grh inhibits premature transcription by occupying Zld binding sites [99]. The co-enrichment of both Zld and Grh motifs in regions gaining accessibility, together with the transcriptional upregulation of both genes, suggests that loss of Rad50 alters the regulatory landscape at loci associated with these pioneer factors.

To further assess whether stage-specific signatures are affected in *rad50* KO CNS, and in line with the GO analysis ("carbohydrate metabolic process," Fig. 4B), we also considered a metabolic pathway previously identified as highly expressed in embryonic but not in larval hemocytes [100]. *Ldh*, coding for lactate dehydrogenase [101, 102], shows strong embryonic enrichment across the three cell types (hemocytes: FC = 50.34; glia: FC = 36.88; neurons: FC = 2.2) (Supplementary Fig. S3D) and is among the most upregulated genes in *rad50* KO CNS in our RNA-seq assay ($\log_2$FC: 2.6, padj: 1.1e−62), which we further confirmed by RT-qPCR (FC: 17.26) (Supplementary Fig. S3E). Furthermore, accessibility at *Ldh* TSS is significantly increased in our ATAC-seq data ($\log_2$FC = 0.66, padj = 1.02e−19) (Fig. 5F). Finally, *in situ* hybridization assays revealed elevated *Ldh* expression levels in *rad50* KO samples compared to controls (Fig. 5G).

Together, the transcriptomic and chromatin accessibility analyses reveal that Rad50 loss leads to changes in gene expression and chromatin accessibility in larval CNS, affecting genes normally highly expressed at the embryonic stage compared to the larval stage (Figs 4A–C, 5A and C–G, and Supplementary Fig. S3D and E). Specific regions enriched for pioneer factor binding motifs show increased accessibility that overlaps with transcriptional changes (Fig. 5B–D). The predominance of gene upregulation and increased chromatin accessibility, coupled with decreased H3K9me2/3 marks observed in polytene chromosomes (Fig. 3 and Supplementary Fig. S2), support a model in which Rad50 contributes to genome regulation during *Drosophila* development.

Discussion

Recent technological advances have enabled unprecedented resolution in defining cell identity. Yet the question of what constitutes a cell type becomes particularly complex in the context of development. Here, we identify a stage-specific signature that accounts for the dominant source of transcriptional variation—surpassing even differences between cell types. Stage-dependent transcriptomic asymmetry, together with proteomic, molecular, and genetic evidence, implicates

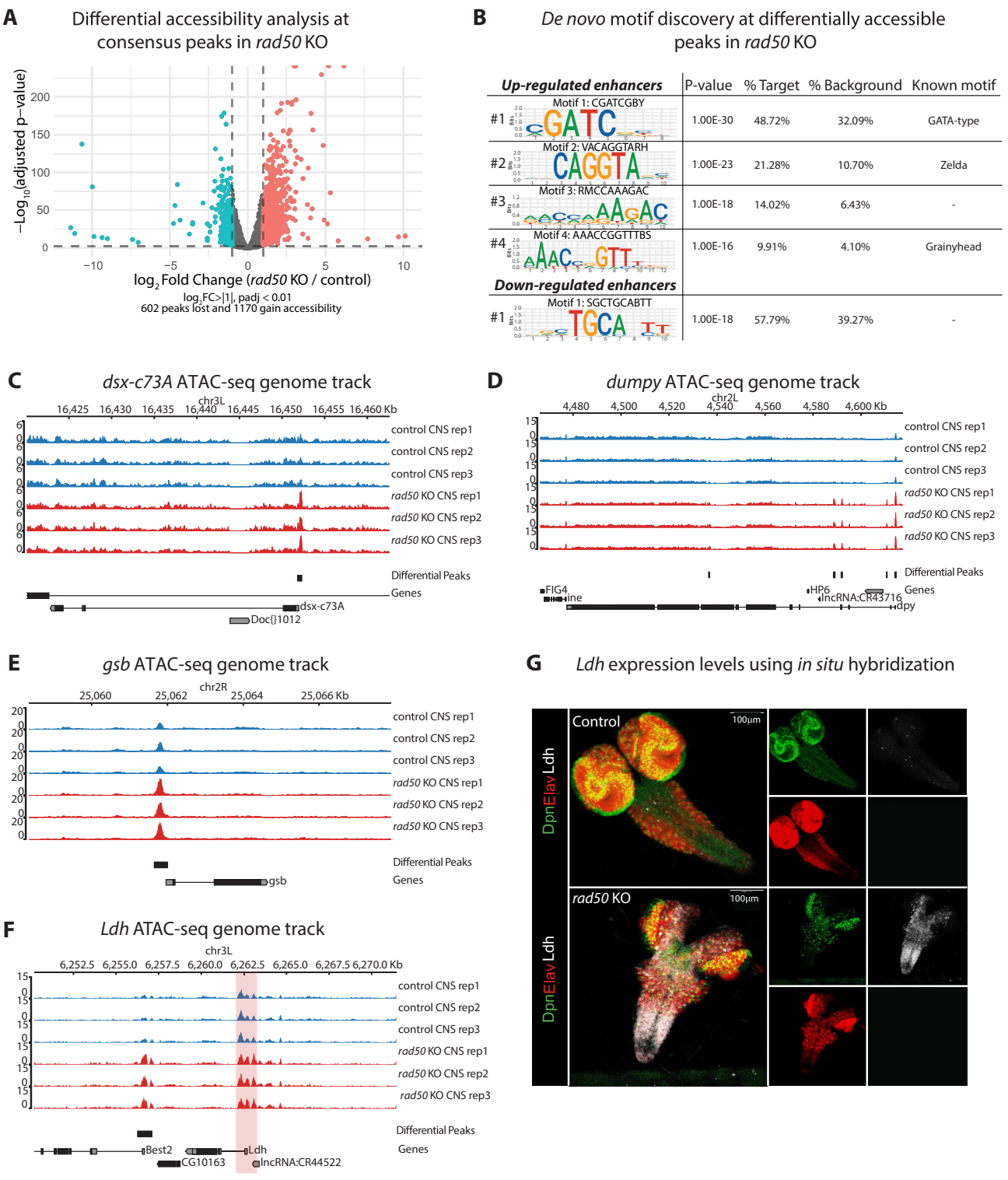

Figure 5. (**A**) Differential accessibility analysis at consensus peaks in *rad50* KO CNS versus control. $|\text{Log}_2\text{FC}| > 1$ and adjusted *P*-value <.01 were used as threshold. (**B**) *De novo* motif discovery at differentially accessible peaks (up or down) over background (all consensus peaks). Significant motifs only shown. (**C**–**E**) Example of genome tracks at differentially accessible genes involved in cuticle development (*dsx-c73A*, *dumpy*, and *gsb*). (**F**) Genome tracks of ATAC-seq signal at *Ldh* locus. (**G**) *In situ* hybridization analysis of *Ldh* expression in control and *rad50* KO CNS. *elav* in red, *deadpan* in green, and *Ldh* in grey. $n \geq 12$.

the contribution of *rad50*, a gene classically associated with DNA repair, in the maintenance of developmentally appropriate chromatin states. These findings align with the emerging paradigm that integrates chromatin architecture, transcriptional programs with the pathways governing DNA replication and repair.

Developmental stage has a predominant effect on cell identity

The bulk RNA-seq assay on embryonic and larval *Drosophila* neurons, hemocytes, and glia highlights the balance between stable cellular identity and developmental plasticity. While core identity genes remain robustly expressed across stages [5], significant transcriptomic rewiring occurs over time. This suggests that developmental signals strongly modulate differentiated cells without compromising their fundamental functions, allowing cells to maintain essential roles while dynamically adapting to stage-specific physiological demands.

Although the stable expression of morphological and functional markers generally defines cell identity, our analysis revealed the dominance of developmental stage over cell type in driving transcriptomic profiles. Embryonic neurons are transcriptionally more similar to embryonic hemocytes and glia than to their larval counterparts, despite neurons and hemocytes sharing neither developmental origin nor function. Hence, the transcriptional landscape of differentiated cells relies on a strong temporal signature, in addition to signatures related to origin and function. In line with these findings, a micro-array analysis on 4028 transcripts within 66 time periods ranging from fertilization to adulthood shows a strong stage-dependent effect [35, 36]. Altogether these data on stage-driven shifts in gene expression challenge a strictly continuous view of the developmental processes. The absence of a shared, cell-type-independent embryonic program is itself biologically informative, likely reflecting dominance of lineage- and differentiation-specific regulatory logic during embryogenesis. By contrast, the smaller set of L3 stage-specific genes converges on shared biological processes, particularly DNA repair and chromatin organization, suggesting that larval cells adopt a common genome maintenance program independently of cell-type identity. Hence, while embryonic cells are trajectory-driven, larval cells converge on a shared maintenance-oriented regulatory state. This finding calls for developmental stages providing an active regulatory dimension of cell identity.

The temporal reorganization of transcriptomes raises important questions about the regulatory mechanisms orchestrating these transitions. The striking magnitude of the stage effect, outweighing even fundamental cell-identity signatures, may indeed reflect the different challenges that embryos and larvae face. Embryos develop in a static, protected environment that prioritizes rapid cell proliferation, lineage specification, and organ development. Larvae, by contrast, hatch into a complex external environment, experiencing changing metabolic demands and exposure to pathogens and environmental stressors.

In the future, the rapidly developing fields of single-cell RNA-seq and spatial transcriptomics will offer the required resolution to study transcriptome-scale effects at cellular and subcellular levels, potentially revealing how temporal and developmental cues combine with local signals from the cellular microenvironment to define cellular identity dynamically.

Loss of Rad50 alters chromatin state and gene expression

Applying DESeq2 [25, 25] with an interaction-term model followed by GO enrichment analysis and RT-qPCR validation, allowed us to extract cell-type-independent stage-specific features, highlighting the DNA repair pathway and in particular Rad50 as a larval-specific feature.

Loss of Rad50 is associated with coordinated changes across multiple chromatin-related processes: differences in histone modification levels, shifts in gene expression, changes in chromatin accessibility. While our study cannot directly establish causality between these phenomena, their coherent relationship suggests that Rad50 influences chromatin dynamics in a fundamental way. This interpretation is supported by the co-IP mass spectrometry analysis, which identifies not only the expected MRN complex partners (Mre11 and Nbs) but also chromatin regulatory proteins including Amun and members of the Myb complex, the transcription initiation factor TFIIB, the histone chaperone Hira and the alpha primase polymerase complex. Such interaction network is consistent with recent studies that have increasingly blurred the traditional boundaries between DNA repair, chromatin organization, and gene expression regulation [20, 69, 70, 73, 76, 103].

Several lines of evidence demonstrate the interconnection between these processes. For example, Topoisomerase IIβ-induced DSBs promote the expression of neuronal early response genes [104]. Rad50 belongs to the structural maintenance of chromosomes (SMC) protein family, whose members—including cohesin and condensin—share structural features and function at the interface of interconnected genome maintenance processes: DNA repair, chromosome segregation, and chromatin architecture [12, 13, 103, 105–107]. Cohesin regulates homology search during DNA repair by organizing chromosomes into local chromatin loops, facilitating the identification of nearby repair templates by the MRX complex and suppressing inter-chromosomal recombination [108]. This loop-based organization is further supported by recent work showing that loop extrusion, mediated by cohesin and condensin, is essential for the formation of γH2AX-marked chromatin domains at DSB sites, creating a platform for efficient repair and maintaining genome stability [109]. Moreover, the spread of γH2AX is not random but is shaped by pre-existing chromosomal contacts and topologically associating domains (TADs), with DSBs near TAD borders generating asymmetric γH2AX domains that can influence repair outcomes[110]. In our mass-spectrometry assay, we did detect interactions between Rad50 and the boundary-associated proteins CTCF and BEAF-32 (Supplementary Table S5) [111, 112]. These findings suggest that DNA repair machinery, chromatin architectural proteins, and transcriptional regulators have coevolved as components of an integrated nuclear ecosystem rather than functioning as independent modules.

In this context, the coordinated chromatin and transcriptional changes observed in *rad50* KO may reflect the disruption of a coherent chromatin state that cannot be fully compensated by proteins with overlapping functions (other DNA repair enzymes with overlapping targets) or structure (other members of SMC-protein family). Notably, the interac-

tion of Rad50 with the alpha-primase polymerase complex and the histone chaperone Hira [60, 63]—both central to replication-coupled chromatin assembly—raises the possibility that Rad50 contributes to the faithful propagation of chromatin states through cell divisions. Perturbation of this process could lead to cumulative changes in the chromatin landscape, consistent with the altered histone modification levels, enhanced chromatin accessibility, and predominantly upregulated gene expression observed in *rad50* mutants. These phenotypes parallel those reported when components of the DNA replication machinery are disrupted, leading to defective transmission of chromatin states. In *C. elegans*, mutation of *div-1*, which encodes a DNA primase subunit, causes a global reduction in repressive histone modifications and widespread derepression of heterochromatic genes [113]. In avian cells, loss of the replication fork-associated factor REV1 impairs the transfer of parental histones during DNA replication, resulting in localized loss of repressive marks and transcriptional derepression [114]. In *Drosophila*, reduced levels of the replication-coupled histone chaperone CAF-1 decrease H3K9 methylation at heterochromatin and impair HP1 recruitment [115, 116]. The convergence of these phenotypes points to a role for Rad50 in maintaining developmentally appropriate chromatin.

In line with this, regions gaining accessibility in *rad50* KO are enriched for binding motifs of Zelda and Grainyhead, two transcription factors involved in both embryonic development [96–99] and larval CNS functions including neuroblast maintenance and Hox-dependent apoptosis [90–95]. Both transcription factors are themselves transcriptionally upregulated upon Rad50 loss, and genes characteristic of embryonic programs are reactivated in L3 mutant CNS. These include cuticle genes, which are canonical Grainyhead targets, and *Ldh* (lactate dehydrogenase), a gene strongly enriched at the embryonic stage across all three cell types and among the most upregulated genes in *rad50* KO CNS. This pattern suggests that Rad50 loss affects the maintenance of chromatin states that normally restrict access to stage-specific regulatory programs. Whether Rad50 contributes to chromatin maintenance through a direct role in replication-coupled chromatin propagation, as suggested by its interaction with the alpha-primase polymerase complex and Hira, or whether the observed changes are secondary consequences of impaired DNA repair accumulating through development, remains to be determined. While future studies will be essential to disentangle these possibilities, the present work highlights the interconnection between chromatin maintenance and DNA replication/repair pathways and its impact in controlling cell identity.

The DNA repair machinery provides a compelling example of protein complexes that have been extensively characterized in the context of a defined biological function. However, recent high-throughput studies are reshaping this classical view, expanding the functional landscape of these complexes beyond DNA repair to encompass DNA replication, chromatin organization and gene regulation. Accordingly, increasing evidence suggest that the impact of DNA repair complexes is modulated by interactions with context-specific partners, many of which are only beginning to be identified. Our work on the *Drosophila rad50* gene supports and extends these emerging insights, providing *in vivo* evidence from an additional animal model and uncovering a previously unappreciated link to cell identity.

Acknowledgements

We thank V. Jungmichel and C. Delaporte for laboratory and experimental support, and the members of the team for fruitful suggestions. We thank the Imaging Center of the IGBMC for technical assistance. The sequencing was performed by the GenomEast platform, a member of the "France Génomique" consortium (ANR 10-INBS-0009). LC–MS/MS was performed with the help of P. Hammam and J. Chicher at the proteomic platform at IBMC, Strasbourg (CNRS FR1589). In addition, stocks obtained from the Bloomington Drosophila Stock Center (NIH P40OD018537) and antibodies obtained from the Developmental Studies Hybridoma Bank created by the NICHD of the NIH and maintained at The University of Iowa (Department of Biology, Iowa City, IA 52242) were used in this study.

Author contribution: Conceptualization, TB, RS, and AG; Methodology, TB, RS, AG, PBC, MM, LC, TM, and MG. Investigation, TB, RS, AG, PBC, MM, LC, TM, and MG. Writing—Original Draft, TB, RS, and AG. Writing—Review and Editing, TB, PBC, and AG. Funding Acquisition, AG, PBC, LC, and TM. Resources, AG; Supervision, AG, and PBC.

Supplementary data

Supplementary data is available at NAR online.

Conflict of interest

None declared.

Funding

This work was supported by INSERM, CNRS, UDS, Ligue Régionale contre le Cancer, Hôpital de Strasbourg, ARC, CEFIPRA, USIAS, and ANR grants, by FRM équipe labélisation, and by IRP CNRS/INSERM/Unistra (Machub). R. Sakr was supported by the French state fund through a doctoral contract from the University of Strasbourg and the Fondation pour la Recherche Médicale (FDT2020010107630). T. Boutet was supported by the French state fund through a doctoral contract from the graduate school IMCbio in Strasbourg and ANR EMAC. The IGBMC was also supported by a French state fund through the ANR labex. L. Ciapponi's lab Sapienza University grant RM120172B7D32C04. T. Mukherjee's lab is supported by the DST-Core Reasearch Grant, DBT-IYBA 2017, CEFIPRA, and USIAS fellowship. Funding to pay the Open Access publication charges for this article was provided by ANR.

Data availability

Sequencing data have been deposited at EBI (E-MTAB-13490, E-MTAB-8702 for RNA-seq, E-MTAB-16072 for ATAC-seq) and are publicly available as of the date of publication. The mass spectrometry proteomics data have been deposited to the ProteomeXchange Consortium via the PRIDE partner repository with the dataset identifier PXD056082 and 10.6019/PXD056082. Scripts for figures and genomic analyses are provided on https://github.com/ThomasBLMN/260611_transcriptomePaper and https://doi.org/10.5281/zenodo.18978512.

References

1. Gulati GS, D'Silva JP, Liu Y *et al.* Profiling cell identity and tissue architecture with single-cell and spatial transcriptomics. *Nat Rev Mol Cell Biol* 2025;26:11–31. https://doi.org/10.1038/s41580-024-00768-2
2. McKinley KL, Castillo-Azofeifa D, Klein OD. Tools and concepts for interrogating and defining cellular identity. *Cell Stem Cell* 2020;26:632–56. https://doi.org/10.1016/j.stem.2020.03.015
3. Morris SA. The evolving concept of cell identity in the single cell era. *Development* 2019;146:dev169748. https://doi.org/10.1242/dev.169748
4. Ye Z, Sarkar CA. Towards a quantitative understanding of cell identity. *Trends Cell Biol* 2018;28:1030–48. https://doi.org/10.1016/j.tcb.2018.09.002
5. Sakr R, Monticelli S, Delaporte C *et al.* NimA promotes cell adhesion at the blood brain barrier of *Drosophila* nervous system. *Embo rep* 2026;27:e728. https://doi.org/10.1038/s44319-026-00728-1
6. Awasaki T, Ito K. Engulfing action of glial cells is required for programmed axon pruning during *Drosophila* metamorphosis. *Curr Biol* 2004;14:668–77. https://doi.org/10.1016/j.cub.2004.04.001
7. Stork T, Engelen D, Krudewig A *et al.* Organization and function of the blood–brain barrier in *Drosophila*. *J Neurosci* 2008;28:587–97. https://doi.org/10.1523/JNEUROSCI.4367-07.2008
8. Volkenhoff A, Weiler A, Letzel M *et al.* Glial glycolysis is essential for neuronal survival in *Drosophila*. *Cell Metab* 2015;22:437–47. https://doi.org/10.1016/j.cmet.2015.07.006
9. Lebestky T, Chang T, Hartenstein V *et al.* Specification of *Drosophila* hematopoietic lineage by conserved transcription factors. *Science* 2000;288:146–9. https://doi.org/10.1126/science.288.5463.146
10. Lemaitre B, Nicolas E, Michaut L *et al.* The dorsoventral regulatory gene cassette spätzle/Toll/cactus controls the potent antifungal response in *Drosophila* adults. *Cell* 1996;86:973–83. https://doi.org/10.1016/S0092-8674(00)80172-5
11. Tepass U, Fessler LI, Aziz A *et al.* Embryonic origin of hemocytes and their relationship to cell death in *Drosophila*. *Development* 1994;120:1829–37. https://doi.org/10.1242/dev.120.7.1829
12. Harvey SH, Krien MJ, O'Connell MJ. Structural maintenance of chromosomes (SMC) proteins, a family of conserved ATPases. *Genome Biol* 2002;3:reviews3003.1. https://doi.org/10.1186/gb-2002-3-2-reviews3003
13. Yoshinaga M, Inagaki Y. Ubiquity and origins of structural maintenance of chromosomes (SMC) proteins in eukaryotes. *Genome Biol Evol* 2021;13:evab256. https://doi.org/10.1093/gbe/evab256
14. Lee LA, Orr-Weaver TL. Regulation of cell cycles in *Drosophila* development: intrinsic and extrinsic cues. *Annu Rev Genet* 2003;37:545–78. https://doi.org/10.1146/annurev.genet.37.110801.143149
15. Ciapponi L, Cenci G, Ducau J *et al.* The *Drosophila* Mre11/Rad50 complex is required to prevent both telomeric fusion and chromosome breakage. *Curr Biol* 2004;14:1360–6. https://doi.org/10.1016/j.cub.2004.07.019
16. Ciapponi L, Cenci G, Gatti M. The *Drosophila* Nbs protein functions in multiple pathways for the maintenance of genome stability. *Genetics* 2006;173:1447–54. https://doi.org/10.1534/genetics.106.058081
17. Oikemus SR, Queiroz-Machado J, Lai K *et al.* Epigenetic telomere protection by *Drosophila* DNA damage response pathways. *PLoS Genet* 2006;2:e71. https://doi.org/10.1371/journal.pgen.0020071
18. Gao G, Bi X, Chen J *et al.* Mre11–Rad50–Nbs complex is required to cap telomeres during *Drosophila* embryogenesis. *Proc Natl Acad Sci USA* 2009;106:10728–33. https://doi.org/10.1073/pnas.0902707106
19. Bosso G, Cipressa F, Moroni ML *et al.* NBS1 interacts with HP1 to ensure genome integrity. *Cell Death Dis* 2019;10:951. https://doi.org/10.1038/s41419-019-2185-x
20. Park H, Cho B, Kim J. Rad50 mediates DNA demethylation to establish pluripotent reprogramming. *Exp Mol Med* 2020;52:1116–27. https://doi.org/10.1038/s12276-020-0467-0
21. Forey R, Barthe A, Tittel-Elmer M *et al.* A role for the Mre11–Rad50–Xrs2 complex in gene expression and chromosome organization. *Mol Cell* 2021;81:183–197. https://doi.org/10.1016/j.molcel.2020.11.010e6.
22. Kim D, Paggi JM, Park C *et al.* Graph-based genome alignment and genotyping with HISAT2 and HISAT-genotype. *Nat Biotechnol* 2019;37:907–15. https://doi.org/10.1038/s41587-019-0201-4
23. Liao Y, Smyth GK, Shi W. featureCounts: an efficient general purpose program for assigning sequence reads to genomic features. *Bioinformatics* 2014;30:923–30. https://doi.org/10.1093/bioinformatics/btt656
24. Anders S, Huber W. Differential expression analysis for sequence count data. *Genome Biol* 2010;11:R106. https://doi.org/10.1186/gb-2010-11-10-r106
25. Love MI, Huber W, Anders S. Moderated estimation of fold change and dispersion for RNA-seq data with DESeq2. *Genome Biol* 2014;15:550. https://doi.org/10.1186/s13059-014-0550-8
26. Zhu A, Ibrahim JG, Love MI. Heavy-tailed prior distributions for sequence count data: removing the noise and preserving large differences. *Bioinformatics* 2019;35:2084–92. https://doi.org/10.1093/bioinformatics/bty895
27. Hoskins RA, Carlson JW, Wan KH *et al.* The Release 6 reference sequence of the *Drosophila melanogaster* genome. *Genome Res* 2015;25:445–58. https://doi.org/10.1101/gr.185579.114
28. Langmead B, Salzberg SL. Fast gapped-read alignment with Bowtie 2. *Nat Methods* 2012;9:357–9. https://doi.org/10.1038/nmeth.1923
29. Quinlan AR, Hall IM. BEDTools: a flexible suite of utilities for comparing genomic features. *Bioinformatics* 2010;26:841–2. https://doi.org/10.1093/bioinformatics/btq033
30. Ramírez F, Dündar F, Diehl S *et al.* deepTools: a flexible platform for exploring deep-sequencing data. *Nucleic Acids Res* 2014;42:W187–91.
31. Heinz S, Benner C, Spann N *et al.* Simple combinations of lineage-determining transcription factors prime *cis*-regulatory elements required for macrophage and B cell identities. *Mol Cell* 2010;38:576–89. https://doi.org/10.1016/j.molcel.2010.05.004
32. Gramates LS, Agapite J, Attrill H *et al.* FlyBase: a guided tour of highlighted features. *Genetics* 2022;220:iyac035. https://doi.org/10.1093/genetics/iyac035
33. Hu Y, Sopko R, Foos M *et al.* FlyPrimerBank: an online database for *Drosophila melanogaster* gene expression analysis and knockdown evaluation of RNAi reagents. *G3 Genes Genomes Genet* 2013;3:1607–16. https://doi.org/10.1534/g3.113.007021
34. Robinson JT, Thorvaldsdottir H, Turner D *et al.* igv.js: an embeddable JavaScript implementation of the Integrative Genomics Viewer (IGV). *Bioinformatics* 2023;39:btac830. https://doi.org/10.1093/bioinformatics/btac830
35. Arbeitman MN, Furlong EEM, Imam F *et al.* Gene expression during the life cycle of *Drosophila melanogaster*. *Science* 2002;297:2270–5. https://doi.org/10.1126/science.1072152
36. Ozerova AM, Gelfand MS. Recapitulation of the embryonic transcriptional program in holometabolous insect pupae. *Sci Rep* 2022;12:17570. https://doi.org/10.1038/s41598-022-22188-y
37. Duda JC, Drenda C, Kästel H *et al.* Benefit of using interaction effects for the analysis of high-dimensional time-response or dose-response data for two-group comparisons. *Sci Rep* 2023;13:20804.
38. Ashburner M, Ball CA, Blake JA *et al.* Gene Ontology: tool for the unification of biology. *Nat Genet* 2000;25:25–9. https://doi.org/10.1038/75556

39. The Gene Ontology Consortium, Aleksander SA, Balhoff J, Carbon S *et al*. The Gene Ontology knowledgebase in 2023. *Genetics* 2023;224:iyad031.
40. Hu Y, Comjean A, Attrill H *et al*. PANGEA: a new gene set enrichment tool for *Drosophila* and common research organisms. *Nucleic Acids Res* 2023;51:W419–26. https://doi.org/10.1093/nar/gkad331
41. Hooper SD, Boué S, Krause R *et al*. Identification of tightly regulated groups of genes during *Drosophila melanogaster* embryogenesis. *Mol Syst Biol* 2007;3:72. https://doi.org/10.1038/msb4100112
42. Papatsenko I, Levine M, Papatsenko D. Temporal waves of coherent gene expression during *Drosophila* embryogenesis. *Bioinformatics* 2010;26:2731–6. https://doi.org/10.1093/bioinformatics/btq513
43. Ostrowski S, Dierick HA, Bejsovec A. Genetic control of cuticle formation during embryonic development of *Drosophila melanogaster*. *Genetics* 2002;161:171–82. https://doi.org/10.1093/genetics/161.1.171
44. Sekelsky J. DNA repair in *Drosophila*: mutagens, models, and missing genes. *Genetics* 2017;205:471–90. https://doi.org/10.1534/genetics.116.186759
45. Johnson-Schlitz DM, Flores C, Engels WR. Multiple-pathway analysis of double-strand break repair mutations in *Drosophila*. *PLoS Genet* 2007;3:e50. https://doi.org/10.1371/journal.pgen.0030050
46. Marek LR, Bale AE. *Drosophila* homologs of FANCD2 and FANCL function in DNA repair. *DNA Repair (Amst)* 2006;5:1317–26. https://doi.org/10.1016/j.dnarep.2006.05.044
47. Melnikova L, Biessmann H, Georgiev P. The Ku protein complex is involved in length regulation of *Drosophila* telomeres. *Genetics* 2005;170:221–35. https://doi.org/10.1534/genetics.104.034538
48. Redon C, Pilch D, Rogakou E *et al*. Histone H2A variants H2AX and H2AZ. *Curr Opin Genet Dev* 2002;12:162–9. https://doi.org/10.1016/S0959-437X(02)00282-4
49. Stormo BM, Fox DT. Polyteny: still a giant player in chromosome research. *Chromosome Res* 2017;25:201–14. https://doi.org/10.1007/s10577-017-9562-z
50. Zhimulev IF, Zykova TY, Goncharov FP *et al*. Genetic organization of interphase chromosome bands and interbands in *Drosophila melanogaster*. *PLoS One* 2014;9:e101631. https://doi.org/10.1371/journal.pone.0101631
51. Stadler MR, Haines JE, Eisen MB. Convergence of topological domain boundaries, insulators, and polytene interbands revealed by high-resolution mapping of chromatin contacts in the early *Drosophila melanogaster* embryo. *eLife* 2017;6:e29550. https://doi.org/10.7554/eLife.29550
52. Banks GR, Boezi JA, Lehman IR. A high molecular weight DNA polymerase from *Drosophila melanogaster* embryos. Purification, structure, and partial characterization. *J Biol Chem* 1979;254:9886–92. https://doi.org/10.1016/S0021-9258(19)83600-1
53. Marygold SJ, Attrill H, Speretta E *et al*. The DNA polymerases of *Drosophila melanogaster*. *Fly* 2020;14:49–61. https://doi.org/10.1080/19336934.2019.1710076
54. McClure AW, Canal B, Diffley JFX. A DNA replication fork-centric view of the budding yeast DNA damage response. *DNA Repair (Amst)* 2022;119:103393. https://doi.org/10.1016/j.dnarep.2022.103393
55. Ashour ME, Mosammaparast N. Mechanisms of damage tolerance and repair during DNA replication. *Nucleic Acids Res* 2021;49:3033–47. https://doi.org/10.1093/nar/gkab101
56. Bryant HE, Petermann E, Schultz N *et al*. PARP is activated at stalled forks to mediate Mre11-dependent replication restart and recombination. *EMBO J* 2009;28:2601–15. https://doi.org/10.1038/emboj.2009.206
57. Delamarre A, Barthe A, De LR *et al*. MRX increases chromatin accessibility at stalled replication forks to promote nascent DNA resection and cohesin loading. *Mol Cell* 2020;77:395–410. https://doi.org/10.1016/j.molcel.2019.10.029
58. Shalaby NA, Parks AL, Morreale EJ *et al*. A screen for modifiers of notch signaling uncovers amun, a protein with a critical role in sensory organ development. *Genetics* 2009;182:1061–76. https://doi.org/10.1534/genetics.108.099986
59. Loza-Coll MA, Southall TD, Sandall SL *et al*. Regulation of *Drosophila* intestinal stem cell maintenance and differentiation by the transcription factor Escargot. *EMBO J* 2014;33:2983–96. https://doi.org/10.15252/embj.201489050
60. Bonnefoy E, Orsi GA, Couble P *et al*. The essential role of *Drosophila* HIRA for *de novo* assembly of paternal chromatin at fertilization. *PLoS Genet* 2007;3:e182. https://doi.org/10.1371/journal.pgen.0030182
61. Zhang L, Liu Q, Liu Y *et al*. Co-profiling of translatome and transcriptome reveals the regulation of dynamic gene expression during *Drosophila* embryogenesis. *ABBS* 2024;56:1711–5, https://doi.org/10.3724/abbs.2024146
62. Schoberleitner I, Bauer I, Huang A *et al*. CHD1 controls H3.3 incorporation in adult brain chromatin to maintain metabolic homeostasis and normal lifespan. *Cell Rep* 2021;37:109769. https://doi.org/10.1016/j.celrep.2021.109769
63. Choi J, Kim T, Cho E-J. HIRA vs. DAXX: the two axes shaping the histone H3.3 landscape. *Exp Mol Med* 2024;56:251–63. https://doi.org/10.1038/s12276-023-01145-3
64. Zhang H, Gan H, Wang Z *et al*. RPA interacts with HIRA and regulates H3.3 deposition at gene regulatory elements in mammalian cells. *Mol Cell* 2017;65:272–84. https://doi.org/10.1016/j.molcel.2016.11.030
65. Lewis PW, Beall EL, Fleischer TC *et al*. Identification of a *Drosophila* Myb-E2F2/RBF transcriptional repressor complex. *Genes Dev* 2004;18:2929–40. https://doi.org/10.1101/gad.1255204
66. DeBruhl H, Wen H, Lipsick JS. The complex containing *Drosophila* Myb and RB/E2F2 regulates cytokinesis in a histone H2Av-dependent manner. *Mol Cell Biol* 2013;33:1809–18. https://doi.org/10.1128/MCB.01401-12
67. Milacic M, Beavers D, Conley P *et al*. The Reactome Pathway Knowledgebase 2024. *Nucleic Acids Res* 2024;52:D672–8. https://doi.org/10.1093/nar/gkad1025
68. Merino ST, Cummings WJ, Acharya SN *et al*. Replication-dependent early meiotic requirement for Spo11 and Rad50. *Proc Natl Acad Sci USA* 2000;97:10477–82. https://doi.org/10.1073/pnas.190346097
69. Salifou K, Burnard C, Basavarajaiah P *et al*. Chromatin-associated MRN complex protects highly transcribing genes from genomic instability. *Sci Adv* 2021;7:eabb2947. https://doi.org/10.1126/sciadv.abb2947
70. Lamaa A, Le Bras M, Skuli N *et al*. A novel cytoprotective function for the DNA repair protein Ku in regulating p53 mRNA translation and function. *EMBO Rep* 2016;17:508–18. https://doi.org/10.15252/embr.201541181
71. Abbasi S, Schild-Poulter C. Mapping the Ku interactome using proximity-dependent biotin identification in human cells. *J Proteome Res* 2019;18:1064–77. https://doi.org/10.1021/acs.jproteome.8b00771
72. Tan Y, Yao L, Gamliel A *et al*. Signal-induced enhancer activation requires Ku70 to read topoisomerase1–DNA covalent complexes. *Nat Struct Mol Biol* 2023;30:148–58. https://doi.org/10.1038/s41594-022-00883-8
73. Kendek A, Sandron A, Lambooij J-P *et al*. DNA double-strand break movement in heterochromatin depends on the histone acetyltransferase dGcn5. *Nucleic Acids Res* 2024;52:11753–67, , https://doi.org/10.1093/nar/gkae775
74. Ramanathan B, Smerdon MJ. Changes in nuclear protein acetylation in u.v.-damaged human cells. *Carcinogenesis* 1986;7:1087–94. https://doi.org/10.1093/carcin/7.7.1087

75. Ramanathan B, Smerdon MJ. Enhanced DNA repair synthesis in hyperacetylated nucleosomes. *J Biol Chem* 1989;264:11026–34. https://doi.org/10.1016/S0021-9258(18)60422-3
76. Dinant C, Houtsmuller AB, Vermeulen W. Chromatin structure and DNA damage repair. *Epigenetics Chromatin* 2008;1:9. https://doi.org/10.1186/1756-8935-1-9
77. Mello JA, Silljé HHW, Roche DMJ *et al.* Human Asf1 and CAF-1 interact and synergize in a repair-coupled nucleosome assembly pathway. *EMBO Rep* 2002;3:329–34. https://doi.org/10.1093/embo-reports/kvf068
78. Polo SE, Roche D, Almouzni G. New histone incorporation marks sites of UV repair in human cells. *Cell* 2006;127:481–93. https://doi.org/10.1016/j.cell.2006.08.049
79. Zhang T, Cooper S, Brockdorff N. The interplay of histone modifications—writers that read. *EMBO Rep* 2015;16:1467–81. https://doi.org/10.15252/embr.201540945
80. Elgin SCR, Reuter G. Position-effect variegation, heterochromatin formation, and gene silencing in *Drosophila*. *Cold Spring Harb Perspect Biol* 2013;5:a017780. https://doi.org/10.1101/cshperspect.a017780
81. Delandre C, Marshall OJ. United colours of chromatin? Developmental genome organisation in flies. *Biochem Soc Trans* 2019;47:691–700. https://doi.org/10.1042/BST20180605
82. Cooper S, Dienstbier M, Hassan R *et al.* Targeting polycomb to pericentric heterochromatin in embryonic stem cells reveals a role for H2AK119u1 in PRC2 recruitment. *Cell Rep* 2014;7:1456–70. https://doi.org/10.1016/j.celrep.2014.04.012
83. Peters AHFM, Kubicek S, Mechtler K *et al.* Partitioning and plasticity of repressive histone methylation states in mammalian chromatin. *Mol Cell* 2003;12:1577–89. https://doi.org/10.1016/S1097-2765(03)00477-5
84. Tosolini M, Brochard V, Adenot P *et al.* Contrasting epigenetic states of heterochromatin in the different types of mouse pluripotent stem cells. *Sci Rep* 2018;8:5776. https://doi.org/10.1038/s41598-018-23822-4
85. Zhang Y, Liu T, Meyer CA *et al.* Model-based Analysis of ChIP-Seq (MACS). *Genome Biol* 2008;9:R137. https://doi.org/10.1186/gb-2008-9-9-r137
86. McDaniel SL, Gibson TJ, Schulz KN *et al.* Continued activity of the pioneer factor Zelda is required to drive zygotic genome activation. *Mol Cell* 2019;74:185–195. https://doi.org/10.1016/j.molcel.2019.01.014
87. Liang H-L, Nien C-Y, Liu H-Y *et al.* The zinc-finger protein Zelda is a key activator of the early zygotic genome in *Drosophila*. *Nature* 2008;456:400–3. https://doi.org/10.1038/nature07388
88. Hamm DC, Harrison MM. Regulatory principles governing the maternal-to-zygotic transition: insights from *Drosophila melanogaster*. *Open Biol* 2018;8:180183. https://doi.org/10.1098/rsob.180183
89. Schulz KN, Bondra ER, Moshe A *et al.* Zelda is differentially required for chromatin accessibility, transcription factor binding, and gene expression in the early *Drosophila* embryo. *Genome Res* 2015;25:1715–26. https://doi.org/10.1101/gr.192682.115
90. Larson ED, Komori H, Gibson TJ *et al.* Cell-type-specific chromatin occupancy by the pioneer factor Zelda drives key developmental transitions in *Drosophila*. *Nat Commun* 2021;12:7153. https://doi.org/10.1038/s41467-021-27506-y
91. Reichardt I, Bonnay F, Steinmann V *et al.* The tumor suppressor Brat controls neuronal stem cell lineages by inhibiting Deadpan and Zelda. *EMBO Rep* 2018;19:102–17. https://doi.org/10.15252/embr.201744188
92. Bakshi A, Sipani R, Ghosh N *et al.* Sequential activation of Notch and Grainyhead gives apoptotic competence to Abdominal-B expressing larval neuroblasts in *Drosophila* central nervous system. *PLoS Genet* 2020;16:e1008976. https://doi.org/10.1371/journal.pgen.1008976
93. Cenci C, Gould AP. *Drosophila* Grainyhead specifies late programmes of neural proliferation by regulating the mitotic activity and Hox-dependent apoptosis of neuroblasts. *Development* 2005;132:3835–45. https://doi.org/10.1242/dev.01932
94. Khandelwal R, Sipani R, Govinda Rajan S *et al.* Combinatorial action of Grainyhead, Extradenticle and Notch in regulating Hox mediated apoptosis in *Drosophila* larval CNS. *PLoS Genet* 2017;13:e1007043. https://doi.org/10.1371/journal.pgen.1007043
95. Sipani R, Rawal Y, Barman J *et al.* *Drosophila* Grainyhead gene and its neural stem cell specific enhancers show epigenetic synchrony in the cells of the central nervous system. *Dev Biol* 2025;522:227–39. https://doi.org/10.1016/j.ydbio.2025.03.012
96. Bray SJ, Kafatos FC. Developmental function of Elf-1: an essential transcription factor during embryogenesis in *Drosophila*. *Genes Dev* 1991;5:1672–83. https://doi.org/10.1101/gad.5.9.1672
97. Jacobs J, Atkins M, Davie K *et al.* The transcription factor Grainy head primes epithelial enhancers for spatiotemporal activation by displacing nucleosomes. *Nat Genet* 2018;50:1011–20. https://doi.org/10.1038/s41588-018-0140-x
98. Nüsslein-Volhard C, Wieschaus E, Kluding H. Mutations affecting the pattern of the larval cuticle in *Drosophila melanogaster*: I. Zygotic loci on the second chromosome. *Wilhelm Roux' Archiv* 1984;193:267–82. https://doi.org/10.1007/BF00848156
99. Harrison MM, Botchan MR, Cline TW. Grainyhead and Zelda compete for binding to the promoters of the earliest-expressed *Drosophila* genes. *Dev Biol* 2010;345:248–55. https://doi.org/10.1016/j.ydbio.2010.06.026
100. Cattenoz PB, Sakr R, Pavlidaki A *et al.* Temporal specificity and heterogeneity of *Drosophila* immune cells. *EMBO J* 2020;39:e104486. https://doi.org/10.15252/embj.2020104486
101. Onoufriou A, Alahiotis SN. *Drosophila* lactate dehydrogenase: molecular and genetic aspects. *Biochem Genet* 1982;20:1195–209. https://doi.org/10.1007/BF00498943
102. Abu-Shumays RL, Fristrom JW. IMP-L3, a 20-hydroxyecdysone-responsive gene encodes *Drosophila* lactate dehydrogenase: structural characterization and developmental studies. *Dev Genet* 1997;20:11–22. https://doi.org/10.1002/(SICI)1520-6408(1997)20:1(11::AID-DVG2)3.0.CO;2-C
103. Oldenkamp R, Rowland BD. A walk through the SMC cycle: from catching DNAs to shaping the genome. *Mol Cell* 2022;82:1616–30. https://doi.org/10.1016/j.molcel.2022.04.006
104. Madabhushi R, Gao F, Pfenning AR *et al.* Activity-induced DNA breaks govern the expression of neuronal early-response genes. *Cell* 2015;161:1592–605. https://doi.org/10.1016/j.cell.2015.05.032
105. Hirano T. At the heart of the chromosome: SMC proteins in action. *Nat Rev Mol Cell Biol* 2006;7:311–22. https://doi.org/10.1038/nrm1909
106. Wu N, Yu H. The Smc complexes in DNA damage response. *Cell Biosci* 2012;2:5. https://doi.org/10.1186/2045-3701-2-5
107. Rutkauskas M, Kim E. In vitro dynamics of DNA loop extrusion by structural maintenance of chromosomes complexes. *Curr Opin Genet Dev* 2025;90:102284. https://doi.org/10.1016/j.gde.2024.102284
108. Piazza A, Bordelet H, Dumont A *et al.* Cohesin regulates homology search during recombinational DNA repair. *Nat Cell Biol* 2021;23:1176–86. https://doi.org/10.1038/s41556-021-00783-x
109. Arnould C, Rocher V, Finoux A-L *et al.* Loop extrusion as a mechanism for formation of DNA damage repair foci. *Nature* 2021;590:660–5. https://doi.org/10.1038/s41586-021-03193-z
110. Collins PL, Purman C, Porter SI *et al.* DNA double-strand breaks induce H2Ax phosphorylation domains in a contact-dependent manner. *Nat Commun* 2020;11:3158. https://doi.org/10.1038/s41467-020-16926-x

111. Schwartz YB, Linder-Basso D, Kharchenko PV *et al.* Nature and function of insulator protein binding sites in the *Drosophila* genome. *Genome Res* 2012;22:2188–98. https://doi.org/10.1101/gr.138156.112
112. Nègre N, Brown CD, Shah PK *et al.* A comprehensive map of insulator elements for the *Drosophila* genome. *PLoS Genet* 2010;6:e1000814.
113. Klosin A, Reis K, Hidalgo-Carcedo C *et al.* Impaired DNA replication derepresses chromatin and generates a transgenerationally inherited epigenetic memory. *Sci Adv* 2017;3:e1701143. https://doi.org/10.1126/sciadv.1701143
114. Sarkies P, Reams C, Simpson LJ *et al.* Epigenetic instability due to defective replication of structured DNA. *Mol Cell* 2010;40:703–13. https://doi.org/10.1016/j.molcel.2010.11.009
115. Huang H, Yu Z, Zhang S *et al.* Drosophila CAF-1 regulates HP1-mediated epigenetic silencing and pericentric heterochromatin stability. *J Cell Sci* 2010;123:2853–61. https://doi.org/10.1242/jcs.063610
116. Song Y, He F, Xie G *et al.* CAF-1 is essential for *Drosophila* development and involved in the maintenance of epigenetic memory. *Dev Biol* 2007;311:213–22. https://doi.org/10.1016/j.ydbio.2007.08.039

Received: December 18, 2025. **Revised:** February 25, 2026. **Accepted:** March 5, 2026